Tracking control of an articulated intervention autonomous underwater vehicle in 6DOF using generalized super-twisting: Theory and experiments

Ida-Louise G. Borlaug, Kristin Y. Pettersen, *Fellow, IEEE*, and Jan Tommy Gravdahl, *Senior member, IEEE*

***Abstract*—The articulated intervention autonomous underwater vehicle (AIAUV) is an underwater swimming manipulator with intervention capabilities. Station-keeping and trajectory tracking are essential for the AIAUV to be able to move in confined spaces and to perform intervention tasks. In this paper, we propose using a generalized super-twisting algorithm (GSTA), which is an extension of the regular super-twisting algorithm, for the trajectory tracking of the position and orientation of the base of the AIAUV in 6DOF. We also propose using a higher-order sliding mode observer (HOSMO) for estimating the linear and angular velocities when velocity measurements are unavailable. Furthermore, we show the ultimate boundedness of the tracking errors for a control law using the GSTA and for a control law that combines the GSTA with a HOSMO. We also prove that the GSTA gives global uniform finite-time stability. Finally, we demonstrate the applicability of the proposed control laws with comprehensive simulation and experimental results.**

***Index Terms*—Autonomous underwater vehicle, Control application, Experimental results, Robotics, Sliding mode control.**

I. Introduction

The articulated intervention autonomous underwater vehicle (AIAUV) is an underwater vehicle with multiple joints, such as a manipulator arm, and multiple thrusters, i.e., an underwater swimming manipulator. The thrusters impart the AIAUV with station-keeping capabilities and enable the AIAUV to perform trajectory tracking without using body undulations, which are necessary for underwater snake robots [1]. The joints enable the AIAUV to operate as a manipulator arm, thus enabling the AIAUV to perform intervention tasks. These manoeuvring capabilities and its slender body enable the AIAUV to move around in confined spaces to which a remotely operated vehicle (ROV) or survey autonomous underwater vehicle would not have access. Moreover, the AIAUV has adopted the high kinematic redundancy of underwater snake robots and the fully energy-efficient hydrodynamic properties and tetherless operation of autonomous underwater vehicles. These properties enable the AIAUV to exploit the full potential of the inherent kinematic redundancy [2], [3].

Station-keeping and trajectory tracking are essential for the AIAUV to be able to move in confined spaces and to perform intervention tasks. Since the AIAUV is a floating base robot manipulator, standard control methods for fixed-base robot manipulators cannot be applied to the AIAUV. Moreover, the AIAUV is subject to hydrodynamic and hydrostatic parameter uncertainties, uncertain thruster characteristics, unknown disturbances, and unmodeled dynamics. Furthermore, since the coupling forces caused by the manipulator joint motion are even larger for the AIAUV than for ROVs because the AIAUV has no separate vehicle base while ROVs have a separate base with a larger inertia compared to the manipulator arm, it is essential for the control approach to be robust. The design of a robust trajectory tracking controller for the AIAUV is therefore the objective of this paper.

Sliding mode control (SMC) is a robust and versatile non-linear control approach that has been used for many different systems and applications, including three-phase power converters [4], Markovian jump systems [5], [6], stochastic systems [7], [8] and microgrid control [9]. For underwater vehicles, SMC has been used for singularity-free control [10], to address partly unknown non-linear thruster characteristics [11], [12] and for trajectory control [13] - [16]. SMC has also been used to handle coupling forces between a manipulator arm and an underwater vehicle [17]. In [18], SMC is applied to land-based snake robots to achieve robust tracking of a desired gait pattern and underactuated straight-line path following.

In recent years, SMC has been developed into higher-order SMC schemes that remove the chattering problem. The super-twisting algorithm (STA) with adaptive gains [19] has been tested for the AIAUV in 2DOF and 6DOF in [20] and [21], respectively, because this algorithm has been considered to be the most powerful second-order continuous SMC algorithm. The STA attenuates chattering, and no conservative upper bound on the disturbance gradient has to be considered to maintain sliding because of the adaptive gains. In [20], tracking control of the centre of mass of the AIAUV in 2D was considered by using STA with adaptive gains [19] and a higher-order sliding mode observer (HOSMO) [22]. It was proven that the tracking errors were ultimately bounded, and the simulation results demonstrated that the proposed control method provided excellent tracking capabilities. The results obtained in [20] were therefore extended to 6DOF in [21]. In [21], the position, orientation and joint angles were considered for the tracking problem, and equally good results were obtained in theory and in simulations. In [20] and [21], a HOSMO had to be used because velocity measurements were unavailable. When using a HOSMO, quaternions cannot be used to represent the system since the HOSMO does not work with a different number of states in position versus velocity.

I.-L. G. Borlaug, K. Y. Pettersen and J. T. Gravdahl are with the Centre for Autonomous Marine Operations and Systems, Department of Engineering Cybernetics, Norwegian University of Science and Technology (NTNU), Trondheim, Norway. (e-mail: {Ida.Louise.Borlaug, Kristin.Y.Pettersen, Jan.Tommy.Gravdahl}@ntnu.no).

In this paper the generalized super-twisting algorithm (GSTA) [23] is used for trajectory tracking in 6DOF. GSTA is an extension of STA that provides finite-time convergence in the presence of time- and state-dependent perturbations, which is essential for robust control of the AIAUV. Preliminary results were presented in [24], where we considered the position, orientation and joint angles for trajectory tracking, but we assumed that velocity measurements were available. We thus avoided using a HOSMO, which means that we could use quaternions to represent the system. We then avoided singularities in the Jacobian matrix at $\theta = \pm\pi/2$, which is a well-known problem when using Euler angles (xyz-convention). Furthermore, we showed the ultimate boundedness of the tracking error, and we illustrated our theoretical findings with simulation results. We also proved that the GSTA is actually globally uniformly finite-time stable, while in [23], the GSTA was proven to be only globally finite-time table. Finally, GSTA was compared with STA with adaptive gains. In this paper, we also consider the case where velocity measurements are unavailable by solving the tracking control problem by using GSTA in combination with a HOSMO [22]. The reason we chose to use the HOSMO is because of its strong stability property. Specifically, the finite-time stability property of the HOSMO enables us to show that the closed-loop system is uniformly globally asymptotically stable. For this purpose, we use Euler angles since we cannot use quaternions when the HOSMO is used. Furthermore, we show the ultimate boundedness of the tracking errors when the HOSMO is included. We also present comprehensive simulation and experimental results that validate and show the applicability of both control laws. The purpose of the experiments is to validate the theory and the robustness of the control approaches, by showing that the proposed approaches also work in experiments and not only in the ideal case presented by simulations. This argument goes for both the GSTA and the HOSMO, as, to the best of the authors knowledge, few experimental results exist for these methods.

The contributions of this paper can be summarized as follows. The trajectory tracking control problem of an AIAUV in 6DOF is solved using GSTA. The tracking errors are proven to be ultimately bounded. Furthermore, the GSTA is proven to give global uniform finite-time stability, whereas in [23], the GSTA was only proven to give global finite-time stability. Comprehensive simulation and experimental results that validate that the approach is well suited for control of an AIAUV are presented. The trajectory tracking control problem of an AIAUV in 6DOF is also solved via GSTA combined with a HOSMO. Additionally, the tracking errors are proven to be ultimately bounded, and comprehensive simulation and experimental results are presented that validate that the approach is well suited for control of an AIAUV.

The remainder of this paper is organized as follows. In Sec. II, the model and the tracking control problem for the AIAUV are defined mathematically. The control law for tracking the desired trajectory is presented in Sec. III. In Sec. IV, we prove the ultimate boundedness of the tracking errors. A description of the simulation model implemented for this paper and the simulation results are presented in Sec. V, and a description of the robot used for the experiments, the set-up and the experimental results are given in Sec. VI. Conclusions and suggestions for future work are given in Sec. VII.

II. Modelling and the tracking control problem

In this section, we present the model and the mathematical definition of the tracking control problem for the AIAUV. The AIAUV is composed of n links connected by $n-1$ motorized joints, where each joint is regarded as a one-dimensional Euclidean joint. We consider link 1 to be the base and link n to be the front, where the end-effector is positioned. Furthermore, the AIAUV is equipped with m thrusters. To provide station-keeping capabilities, it has tunnel thrusters acting through the links, and to provide forward thrust, it has one or more thrusters acting along the body of the AIAUV. For control purposes, the AIAUV is considered to be a floating-base manipulator operating in an underwater environment, subject to added mass forces, dissipative drag forces, and gravity and buoyancy forces. This allows us to model the AIAUV as an underwater vehicle manipulator system (UVMS), with dynamic equations given in matrix form as [25], [26]

$$M(q)\dot{\zeta} + C(q,\zeta)\zeta + D(q,\zeta)\zeta + g(q, R_B^I) = \tau(q) \quad (1)$$

where $q \in \mathbb{R}^{(n-1)}$ is the vector representing the joint angles, $M(q)$ is the inertia matrix including added mass terms, $C(q,\zeta)$ is the Coriolis-centripetal matrix, $D(q,\zeta)$ is the damping matrix, and $g(q, R_B^I)$ is the matrix of gravitational and buoyancy forces. The control input is given by the generalized forces:

$$\tau(q) = \begin{bmatrix} T(q) & 0_{6\times(n-1)} \\ 0_{(n-1)\times m} & I_{(n-1)\times(n-1)} \end{bmatrix} \begin{bmatrix} \tau_{thr} \\ \tau_q \end{bmatrix} \quad (2)$$

where $T(q) \in \mathbb{R}^{6\times m}$ is the thruster configuration matrix, $\tau_{thr} \in \mathbb{R}^m$ is the vector of thruster forces, and $\tau_q \in \mathbb{R}^{(n-1)}$ represents the joint torques. To implement the control input, a thruster allocation scheme as proposed in [27] needs to be implemented to distribute the desired control inputs onto the thrusters. The vector of body-fixed velocities, ζ, is defined as

$$\zeta = \begin{bmatrix} v^T & \omega^T & \dot{q}^T \end{bmatrix}^T \in \mathbb{R}^{6+(n-1)} \quad (3)$$

where v and ω are the body-fixed linear and angular velocities of the base of the AIAUV and $\dot{q}$ is the vector of joint angle velocities. In [21], we used Euler angles to represent the orientation of the AIAUV, and in [24], we used quaternions. In this paper, we use both Euler angles and quaternions to represent the orientation. Specifically, we use quaternions when the HOSMO is not used and Euler angles when the HOSMO is used. The reason for this choice is that the HOSMO does not work with quaternions; finding a HOSMO that works with quaternions is a task for future work.

A. Model represented using quaternions

In this section, the model represented using quaternions will be described. By using quaternions, we can avoid singularities in the Jacobian matrix at $\theta = \pm\pi/2$, which is a well-known problem when using Euler angles (xyz-convention). Using Euler parameters rather than Euler angles thus provides us the advantage of a well-defined Jacobian matrix, which

is necessary to be able to use the inverse of the Jacobian matrix. However, at the same time, we cannot use the HOSMO from [22], which means that we need velocity measurements to control the system. The complete state vector specifying the position, orientation, and shape of the AIAUV is then represented as

$$\xi = \begin{bmatrix}\eta_1^T & p^T & q^T\end{bmatrix}^T \quad \in \mathbb{R}^{7+(n-1)} \tag{4}$$

where $\eta_1 = \begin{bmatrix}x & y & z\end{bmatrix}^T \in \mathbb{R}^3$ is the position of the base and $p = \begin{bmatrix}\varepsilon^T & \eta\end{bmatrix}^T = \begin{bmatrix}\varepsilon_1 & \varepsilon_2 & \varepsilon_3 & \eta\end{bmatrix}^T \in \mathbb{R}^4$ is the unit quaternion describing the orientation of the base in the inertial frame. The Euler parameters η and ε satisfy

$$\eta^2 + \varepsilon^T\varepsilon = 1. \tag{5}$$

The kinematic differential equation for the unit quaternion can be written as in [25] as

$$\begin{bmatrix}\dot{\varepsilon}\\ \dot{\eta}\end{bmatrix} = \frac{1}{2}\begin{bmatrix}\eta I_3 + S(\varepsilon)\\ -\varepsilon^T\end{bmatrix}\omega = J_{k,oq}(p)\omega \tag{6}$$

where I_3 is the (3×3) identity matrix and $S(\cdot)$ is the cross-product operator defined as in [28, Definition 2.2]. To complete the dynamic model, we can write the relationship between the body-fixed velocities and the complete state vector specifying the position, orientation, and shape of the AIAUV as

$$\dot{\xi} = J(p)\zeta = \begin{bmatrix}R_B^I(p) & 0_{3\times 3} & 0_{3\times(n-1)}\\ 0_{4\times 3} & J_{k,oq}(p) & 0_{4\times(n-1)}\\ 0_{(n-1)\times 3} & 0_{(n-1)\times 3} & I_{(n-1)\times(n-1)}\end{bmatrix}\zeta \tag{7}$$

where R_I^B is the rotation matrix expressing the transformation from the inertial frame to the body-fixed frame.

The desired velocities are denoted as

$$\zeta_d = \begin{bmatrix}v_d^T & \omega_d^T & \dot{q}_d^T\end{bmatrix}^T \tag{8}$$

in the body-fixed frame. The desired velocities, ζ_d, are typically given by the inverse kinematics, as described in [29]. The desired trajectory, $\begin{bmatrix}\eta_{1,d}^T & p_d^T & q_d^T\end{bmatrix}^T$, can then be reconstructed from the desired velocity using, for instance, a CLIK algorithm [30, Ch. 11]. The desired orientation of the base of the AIAUV with respect to the inertial reference frame is given by the unit quaternion, $p_d = \begin{bmatrix}\varepsilon_d^T & \eta_d\end{bmatrix}^T$, and the corresponding rotation matrix $R(p_d)$. The orientation error can then be specified by the composite rotation

$$R^T(p_d)R(p) = R(\tilde{p}) \tag{9}$$

where

$$\tilde{p} = \begin{bmatrix}\tilde{\varepsilon}\\ \tilde{\eta}\end{bmatrix} = \begin{bmatrix}\eta\varepsilon_d - \eta_d\varepsilon + S(\varepsilon_d)\varepsilon\\ \eta\eta_d + \varepsilon^T\varepsilon_d\end{bmatrix} \tag{10}$$

is the unit quaternion representing the orientation error. For the orientation, the aim is to ensure that $p = \pm p_d$, which corresponds to $\tilde{p} = \begin{bmatrix}0_{1\times 3} & \pm 1\end{bmatrix}^T$. The tracking errors then consist of the position error $\tilde{\eta}_1$, the orientation error $\tilde{\varepsilon}$ and the joint angle error $\tilde{q}$, and the tracking error vector is then

$$\tilde{\xi} = \begin{bmatrix}\tilde{\eta}_1\\ \tilde{\varepsilon}\\ \tilde{q}\end{bmatrix} = \begin{bmatrix}\eta_1 - \eta_{1,d}\\ \eta\varepsilon_d - \eta_d\varepsilon + S(\varepsilon_d)\varepsilon\\ q - q_d\end{bmatrix}. \tag{11}$$

The goal of the tracking problem is to make the error vector, $\tilde{\xi}$, converge to zero. The tracking control objective is therefore to make $(\tilde{\xi}, \tilde{\zeta}) = (0, 0)$ an asymptotically stable equilibrium point of (1) and (7), which will ensure that the tracking error will converge to zero. Note that $\tilde{\eta}$ is not included as an independent state in (11) since $\tilde{\eta}$ and $\tilde{\varepsilon}$ satisfy (5). When $\tilde{\varepsilon} \to 0$, then $\tilde{p} = \begin{bmatrix}0_{1\times 3} & \pm 1\end{bmatrix}^T$.

B. Model represented using Euler angles

In this section, the model represented using Euler angles will be described. The Jacobian matrix can become singular, but we can then use the HOSMO from [22], which means that we do not require velocity measurements to control the system. The complete state vector specifying the position, orientation, and shape of the AIAUV is represented as

$$\xi = \begin{bmatrix}\eta_1^T & \eta_2^T & q^T\end{bmatrix}^T, \quad \in \mathbb{R}^{6+(n-1)} \tag{12}$$

where $\eta_1 = \begin{bmatrix}x & y & z\end{bmatrix}^T \in \mathbb{R}^3$ is the position of the base and $\eta_2 = \begin{bmatrix}\phi & \theta & \psi\end{bmatrix}^T \in \mathbb{R}^3$ are the Euler angles describing the orientation of the base in the inertial frame. To complete the dynamic model, we can write the relationship between the body-fixed velocities and the complete state vector as

$$\dot{\xi} = J(\eta_2)\zeta = \begin{bmatrix}R_B^I & 0_{3\times 3} & 0_{3\times(n-1)}\\ 0_{3\times 3} & J_{k,o}^{-1} & 0_{3\times(n-1)}\\ 0_{(n-1)\times 3} & 0_{(n-1)\times 3} & I_{(n-1)\times(n-1)}\end{bmatrix}\zeta \tag{13}$$

where $J_{k,o}$ is the Jacobian matrix. The desired velocities are defined as in (8), and the desired trajectories are defined as $\xi_d = \begin{bmatrix}\eta_{1,d}^T & \eta_{2,d}^T & q_d^T\end{bmatrix}^T$. The vector of tracking errors is then

$$\tilde{\xi} = \begin{bmatrix}\tilde{\eta}_1\\ \tilde{\eta}_2\\ \tilde{q}\end{bmatrix} = \begin{bmatrix}\eta_1 - \eta_{1,d}\\ \eta_2 - \eta_{2,d}\\ q - q_d\end{bmatrix}. \tag{14}$$

The goal of the tracking problem is to make the error vector, $\tilde{\xi}$, converge to zero. The tracking control objective is therefore to make $(\tilde{\xi}, \tilde{\zeta}) = (0, 0)$ an asymptotically stable equilibrium point of (1) and (13), which will ensure that the tracking errors will converge to zero.

III. Sliding Mode Control

In this section, we propose two tracking control laws for the AIAUV based on SMC: first, we present one control law where we use the GSTA; then, we present a control law where the GSTA is combined with a HOSMO.

A. Control law using the generalized super-twisting algorithm

In this subsection, the tracking control law for the AIAUV using the GSTA will be presented.

1) Error dynamics: Define $\tilde{x}_1 = \tilde{\xi}$, where $\tilde{\xi}$ is given by (11) and

$$\begin{aligned}\tilde{x}_2 &= \begin{bmatrix}R_B^I(\tilde{p}) & 0_{3\times 3} & 0_{3\times(n-1)}\\ 0_{3\times 3} & \frac{1}{2}(\tilde{\eta}I_3 + S(\tilde{\varepsilon})) & 0_{3\times(n-1)}\\ 0_{(n-1)\times 3} & 0_{(n-1)\times 3} & I_{(n-1)\times(n-1)}\end{bmatrix}(\zeta - \zeta_d)\\ &= T(\tilde{p})\tilde{\zeta}\end{aligned} \tag{15}$$

where ζ and ζ_d are defined in (3) and (8), respectively. The reason for choosing $\tilde{x}_2 = T(\cdot)\tilde{\zeta}$ is that this makes $\tilde{x}_2 = \dot{\tilde{x}}_1$, and by using that, we can prove that the error variables

asymptotically converge to zero when the sliding surface is equal to zero (see Sec. III-A2 for the proof), which is a requirement when designing the sliding surface. If $\tilde{x}_2$ was chosen to be equal to $\tilde{\zeta}$, then this would not have been the case. By differentiating (11) and (15) and using $\dot{\zeta}$ from (1) and $\dot{\xi}$ from (7), the error dynamics is

$$\begin{aligned}
&\dot{\tilde{x}}_1 = \tilde{x}_2 \\
&\dot{\tilde{x}}_2 = \frac{d}{dt}\big(T(\tilde{p})\big)T^{-1}(\tilde{p})\tilde{x}_2 + M^{-1}(\tilde{q}+q_d)T(\tilde{p}) \\
&\Big(- C\big(\tilde{q}+q_d, T^{-1}(\tilde{p})\tilde{x}_2 + \zeta_d\big)\big(T^{-1}(\tilde{p})\tilde{x}_2 + \zeta_d\big) - \\
&D\big(\tilde{q}+q_d, T^{-1}(\tilde{p})\tilde{x}_2 + \zeta_d\big)\big(T^{-1}(\tilde{p})\tilde{x}_2 + \zeta_d\big) - \\
&g(\tilde{q}+q_d, R_B^I) + \tau(\tilde{q}+q_d) - M(\tilde{q}+q_d)\dot{\zeta}_d\Big).
\end{aligned} \tag{16}$$

To reduce the space used to write the error dynamics, we will introduce some new functions, $f_1(\cdot) = \frac{d}{dt}(T(\cdot))T^{-1}(\cdot)$ and $f_2(\cdot) = -C(\cdot)(T^{-1}(\cdot)\tilde{x}_2 + \zeta_d) - D(\cdot)(T^{-1}(\cdot)\tilde{x}_2 + \zeta_d) - g(\cdot) - M(\cdot)\dot{\zeta}_d$, such that the error dynamics can be written as

$$\begin{aligned}
\dot{\tilde{x}}_1 &= \tilde{x}_2 \\
\dot{\tilde{x}}_2 &= f_1(\cdot)\tilde{x}_2 + M^{-1}(\cdot)T(\cdot)\big(f_2(\cdot) + \tau(\cdot)\big)
\end{aligned} \tag{17}$$

2) Sliding surface: To use an SMC approach, we must first design a sliding surface. The sliding surface should be designed such that when the sliding variable σ goes to zero, the error variables asymptotically converge to zero and such that the control input $\tau(\cdot)$ appears in the first derivative of σ. The sliding surface is chosen as

$$\sigma = \tilde{x}_1 + \tilde{x}_2 \quad \in \mathbb{R}^{6+(n-1)}. \tag{18}$$

If $\sigma = 0$, we will have $\tilde{x}_1 + \tilde{x}_2 = 0$. Since $\tilde{x}_2 = \dot{\tilde{x}}_1$, we can write this as

$$\dot{\tilde{x}}_1 = -\tilde{x}_1 \tag{19}$$

which ensures that $\tilde{x}_1$ globally exponentially converges to zero. Since $\tilde{x}_1 = \tilde{\xi}$, the original state variable $\tilde{\xi}$ will also globally exponentially converge to zero if $\sigma = 0$. GSTA, which is described in Sec. III-A3, is then used to drive the sliding surface to zero.

3) Generalized super-twisting algorithm: In this section, the equations describing GSTA are presented in detail. The GSTA proposed in [23] can be written as

$$\begin{aligned}
u_{\mathrm{GSTA}} &= -k_1\phi_1(\sigma) + z \quad \in \mathbb{R}^{6+(n-1)} \\
\dot{z} &= -k_2\phi_2(\sigma)
\end{aligned} \tag{20}$$

where

$$\begin{aligned}
\phi_1(\sigma) &= \lceil\sigma\rfloor^{\frac{1}{2}} + \beta_{\mathrm{GSTA}}\sigma \\
\phi_2(\sigma) &= \frac{1}{2}\lceil\sigma\rfloor^0 + \frac{3}{2}\beta_{\mathrm{GSTA}}\lceil\sigma\rfloor^{\frac{1}{2}} + \beta_{\mathrm{GSTA}}^2\sigma
\end{aligned} \tag{21}$$

where $\lceil a\rfloor^b = |a|^b\,\mathrm{sgn}(a)$ and $k_1 \in \mathbb{R}^{6+(n-1)}$, $k_2 \in \mathbb{R}^{6+(n-1)}$ and $\beta_{\mathrm{GSTA}} \in \mathbb{R}^{6+(n-1)}$ are controller gains. With the extra linear term, compared to STA, three degrees of freedom are obtained in the design of GSTA gains: k_1, k_2 and β_{GSTA}. The linear growth term $\beta_{\mathrm{GSTA}}\sigma$ in ϕ_1 helps to counteract the effects of state-dependent perturbations, which can exponentially increase in time. By choosing the gains as described in [23], the algorithm is proven to make σ go to zero, globally and in finite time, in the presence of state- and time-dependent uncertain control coefficients and perturbations. Note that the gains, when chosen as described in [23], are defined based on bounds on the perturbations.

4) Control input: In this section, we design a control law based on the GSTA described in Sec. III-A3, which we show achieves the tracking control objective in Sec. IV-A. By using the fact that $\dot{\tilde{x}}_1 = \tilde{x}_2$ from (16), (18) can be written as

$$\dot{\tilde{x}}_1 = \sigma - \tilde{x}_1. \tag{22}$$

By differentiating (18), we obtain

$$\dot{\sigma} = \dot{\tilde{x}}_1 + \dot{\tilde{x}}_2 = \tilde{x}_2 + f_1(\cdot)\tilde{x}_2 + M^{-1}(\cdot)T(\cdot)\big(f_2(\cdot) + \tau(\cdot)\big) \tag{23}$$

and by using $\tilde{x}_2 = \sigma - \tilde{x}_1$, we obtain

$$\dot{\sigma} = \sigma - \tilde{x}_1 + f_1(\cdot)(\sigma + \tilde{x}_1) + M^{-1}(\cdot)T(\cdot)\big(f_2(\cdot) + \tau(\cdot)\big). \tag{24}$$

Now, we want the control input $\tau(\cdot)$ to be chosen such that $\dot{\sigma} = u_{\mathrm{GSTA}}$, such that σ and $\dot{\sigma}$ reach zero in finite time. However, since we do not know $f_1(\cdot)$ and $f_2(\cdot)$, we choose our control input to be

$$\tau(\cdot) = T^{-1}(\cdot)u_{\mathrm{GSTA}} \tag{25}$$

and in Sec. IV-A, we will show that this control input achieves the tracking control objective.

B. Control law using the generalized super-twisting algorithm combined with a higher-order sliding mode observer

In this subsection, the tracking control law for the AIAUV using the GSTA combined with the HOSMO will be presented.

1) Third-order sliding mode observer: Because velocity measurements are unavailable, a HOSMO will be developed in this subsection for state estimation. We want to use the third-order SMO presented in [22] because the third-order SMO has been proven to be finite-time stable in [31]. To use this HOSMO, we introduce a change of variables. Define $x_1 = \xi$, where ξ is given by (12), and $x_2 = J(\eta_2)\zeta$, where $J(\eta_2)\zeta$ is given by (13); then, the dynamics can be written as

$$\begin{aligned}
&\dot{x}_1 = x_2 \\
&\dot{x}_2 = \frac{d}{dt}(J(\eta_2))J^{-1}(\eta_2)x_2 + M^{-1}(q)J(\eta_2) \\
&\big(- C\big(q, J^{-1}(\eta_2)x_2\big)J^{-1}(\eta_2)x_2 \\
&- D\big(q, J^{-1}(\eta_2)x_2\big)J^{-1}(\eta_2)x_2 - g(q, R_B^I) + \tau(q)\big)
\end{aligned} \tag{26}$$

Since $\frac{d}{dt}(J(\cdot))$ is well defined and small, we will consider $\frac{d}{dt}(J(\cdot))J^{-1}(\cdot)x_2$ to be a small bounded disturbance called $d(t)$, and we also introduce a new function $f(\cdot) = -C(\cdot)J^{-1}(\cdot)x_2 - D(\cdot)J^{-1}(\cdot)x_2 - g(\cdot)$ to reduce the space used to write the model. The model can then be written as

$$\begin{aligned}
\dot{x}_1 &= x_2 \\
\dot{x}_2 &= d(t) + M^{-1}(\cdot)J(\cdot)\big(f(\cdot) + \tau(\cdot)\big)
\end{aligned} \tag{27}$$

Now that we have introduced the change of variables, the HOSMO can be introduced. By designing the HOSMO structure as in [22], the HOSMO is chosen as

$$\begin{aligned}
\dot{\hat{x}}_1 &= \hat{x}_2 + z_1, & z_1 &= k_1|e_1|^{2/3}\,\mathrm{sgn}(e_1) \\
\dot{\hat{x}}_2 &= \hat{x}_3 + z_2 + M^{-1}(\cdot)J(\cdot)\tau(\cdot), & z_2 &= k_2|e_1|^{1/3}\,\mathrm{sgn}(e_1) \\
\dot{\hat{x}}_3 &= z_3, & z_3 &= k_3\,\mathrm{sgn}(e_1)
\end{aligned} \tag{28}$$

where $k_1 \in \mathbb{R}^{6+(n-1)}$, $k_2 \in \mathbb{R}^{6+(n-1)}$ and $k_3 \in \mathbb{R}^{6+(n-1)}$ are gains to be chosen according to [32] and [33], where $e_1 = x_1 - \hat{x}_1 \in \mathbb{R}^{6+(n-1)}$. One choice of parameters that satisfies the requirements in [32] and [33] is, according to [34], $k_1 = 6L^{1/3}$, $k_2 = 11L^{1/2}$ and $k_3 = 6L$, where $L \in \mathbb{R}^{6+(n-1)}$ is a sufficiently large constant. By defining $e_2 = x_2 - \hat{x}_2$ and $e_3 = -\hat{x}_3 + F(\cdot)$, where $F(\cdot) = d(t) + M^{-1}(\cdot)J(\cdot)f(\cdot)$, the error dynamics of the HOSMO can be written as

$$\begin{aligned} \dot{e}_1 &= -k_1|e_1|^{2/3}\operatorname{sgn}(e_1) + e_2 \\ \dot{e}_2 &= -k_2|e_1|^{1/3}\operatorname{sgn}(e_1) + e_3. \\ \dot{e}_3 &= -k_3\operatorname{sgn}(e_1) + \dot{F}(\cdot) \end{aligned} \tag{29}$$

If $|\dot{F}(\cdot)| < \Delta$, then the HOSMO errors go to zero in finite time [31]. Since $F(\cdot)$ is a combination of $d(t)$, $C(\cdot)J^{-1}(\cdot)x_2$, $D(\cdot)J^{-1}(\cdot)x_2$ and $g(\cdot)$, and since the AIAUV is a mechanical system, these matrices will not change infinitely fast. Therefore, assuming that $\dot{F}(\cdot)$ is bounded is a valid assumption.

2) Sliding surface: As previously discussed, to use an SMC approach, we must first design a sliding surface. The sliding surface should be designed such that when the sliding variable σ goes to zero, the state variables asymptotically converge to zero and such that the control input $\tau(\cdot)$ appears in the first derivative of σ. If we had velocity measurements available, we would choose the sliding surface as

$$\sigma = \tilde{x}_1 + \tilde{x}_2, \quad \in \mathbb{R}^{6+(n-1)} \tag{30}$$

where $\tilde{x}_1 = x_1 - x_{1,d} = \tilde{\xi}$ and $\tilde{x}_2 = x_2 - x_{2,d} = J(\eta_2)\zeta - J(\eta_{2,d})\zeta_d$. Now, if $\sigma = 0$, we will have $\tilde{x}_1 + \tilde{x}_2 = 0$. Since $\tilde{x}_2 = x_2 - x_{2,d} = \dot{x}_1 - \dot{x}_{1,d} = \dot{\tilde{x}}_1$, we can write this as

$$\dot{\tilde{x}}_1 = -\tilde{x}_1 \tag{31}$$

which will ensure that $\tilde{x}_1$ globally exponentially converges to zero. Now, since $\tilde{x}_1 = \tilde{\xi}$, the state variables $\tilde{\xi}$ will also globally exponentially converge to zero if $\sigma = 0$. Since the velocity measurement is not available, the observed state values are used, and we can therefore write the sliding surface with the observed values as

$$\hat{\sigma} = \hat{\tilde{x}}_1 + \hat{\tilde{x}}_2, \quad \in \mathbb{R}^{6+(n-1)} \tag{32}$$

where $\hat{\tilde{x}}_1 = \hat{x}_1 - x_{1,d}$ and $\hat{\tilde{x}}_2 = \hat{x}_2 - x_{2,d}$. Since the HOSMO errors in (29) go to zero in finite time, $\hat{\sigma} = \sigma$ after some finite time. Thus, if $\hat{\sigma} = 0$, the tracking objective will be satisfied.

3) Control input: In this section, we will design a control law based on the GSTA described in Sec. III-A3, which we will show achieves the tracking control objective in Sec. IV-B. By designing the control input $\tau(\cdot)$ such that $\dot{\hat{\sigma}} = u_{\text{GSTA}}$, we thus achieve that $\hat{\sigma}$ and $\dot{\hat{\sigma}}$ reach zero in finite time since the GSTA is finite-time stable. Taking the time derivative of (32) and substituting $\dot{\hat{x}}_1$ and $\dot{\hat{x}}_2$, defined in (28), we find that

$$\begin{aligned} \dot{\hat{\sigma}} = \dot{\hat{\tilde{x}}}_1 + \dot{\hat{\tilde{x}}}_2 = \dot{\hat{x}}_1 - \dot{x}_{1,d} + \dot{\hat{x}}_2 - \dot{x}_{2,d} = \hat{x}_2 + z_1 - \\ \dot{x}_{1,d} + \hat{x}_3 + z_2 + M^{-1}(\cdot)J(\cdot)\tau(\cdot) - \dot{x}_{2,d} \end{aligned} \tag{33}$$

By choosing $\tau(\cdot)$ to be

$$\begin{aligned} \tau(\cdot) = & J^{-1}(\cdot)M(\cdot)\big(- \hat{x}_2 - z_1 + \dot{x}_{1,d} - \hat{x}_3 - \\ & z_2 + \dot{x}_{2,d} + u_{\text{GSTA}}\big) \end{aligned} \tag{34}$$

we obtain

$$\dot{\hat{\sigma}} = u_{\text{GSTA}}. \tag{35}$$

IV. Stability analysis

In this section, we will analyse the closed-loop system resulting from the control laws proposed in Sec. III-A and Sec. III-B, and we show that the tracking error converges asymptotically to zero for both cases.

A. System with the control law from Sec. III-A

In this section, the system with the control law proposed in Sec. III-A, i.e., without the HOSMO, will be analysed. Parts of the analysis build upon the results obtained in [23], but we extend these results by proving uniformity for the GSTA, which makes it possible to show the ultimate boundedness of the tracking errors for the complete system.

1) Overall closed-loop dynamics: By introducing $\varphi(\sigma, \tilde{x}_1, t) = \varphi_1(\sigma, \tilde{x}_1, t) + \varphi_2(\sigma, \tilde{x}_1, t)$, where $\varphi_1(0, \tilde{x}_1, t) = 0$, $\Gamma(\cdot) = M^{-1}(\cdot)$, and using $\tau(\cdot)$ as in (25), we can rewrite (24) as

$$\dot{\sigma} = -k_1\Gamma(\cdot)\phi_1(\sigma) + \varphi_1(\sigma, \tilde{x}_1, t) + \Gamma(\cdot)\big(z + \Gamma^{-1}(\cdot)\varphi_2(\sigma, \tilde{x}_1, t)\big) \tag{36}$$

where $\varphi_1(\sigma, \tilde{x}_1, t) = \sigma + f_1(\cdot)\sigma + \Gamma(\cdot)(-C(\cdot)\sigma - D(\cdot)\sigma)$ and $\varphi_2(\sigma, \tilde{x}_1, t) = -\tilde{x}_1 + f_1(\cdot)\tilde{x}_1 + \Gamma(\cdot)(-C(\cdot)(\tilde{x}_1 + T(\cdot)\zeta_d) - D(\cdot)(\tilde{x}_1 + T(\cdot)\zeta_d) - T(\cdot)g(\cdot) - T(\cdot)M(\cdot)\dot{\zeta}_d)$. Then, by means of (22) and setting $\sigma_1 = \sigma$ and $\sigma_2 = z + \Gamma^{-1}(\cdot)\varphi_2(\sigma, \tilde{x}_1, t)$, we can write the overall closed-loop dynamics as

$$\begin{aligned} &\sum\nolimits_1 \Big\{ \ \dot{\tilde{x}}_1 = -\tilde{x}_1 + \sigma_1 \\ &\sum\nolimits_2 \begin{cases} \dot{\sigma}_1 = -k_1\Gamma(\cdot)\phi_1(\sigma_1) + \varphi_1(\sigma_1, \tilde{x}_1, t) + \Gamma(\cdot)\sigma_2 \\ \dot{\sigma}_2 = -k_2\phi_2(\sigma_1) + \frac{d}{dt}\big(\Gamma^{-1}(\cdot)\varphi_2(\sigma_1, \tilde{x}_1, t)\big) \end{cases} \end{aligned} \tag{37}$$

2) Stability analysis:

Theorem 1: Consider the error dynamics given by (16), and let the sliding surface σ be defined by (18). Let the control input be given by (25). Then, the closed-loop dynamics is described by (37), and the origin of this cascade system is uniformly globally asymptotically stable (UGAS), which ensures the asymptotic convergence of the tracking error when $0 < k_m I \leq \Gamma(\cdot) \leq k_M I$, $|\varphi_1(\cdot)| \leq \alpha|\phi_1(\sigma)|$ and $|\frac{d}{dt}(\Gamma^{-1}(\cdot)\varphi_2(\cdot))| \leq \Delta$, where k_m, k_M, α and Δ are positive constants.

Proof: To analyse the cascade system (37), [35, Lemma 2.1] will be used. Note that the system is actually interconnected, but since subsystem 1 is well behaved as long as σ does not explode, i.e. $\tilde{x}_1$ is bounded, the system can be analysed with cascaded theory by analysing along the trajectories with $\tilde{x}_1(t)$ bounded. When analysing the complete system, we will prove that this is indeed the case, i.e. prove that $\tilde{x}_1(t)$ is uniformly globally bounded. We first start by analysing subsystem 1 without perturbations.

Analysis of subsystem 1 with $\sigma_1 = 0$: With $\sigma_1 = 0$, subsystem 1 can be written as

$$\sum\nolimits_1 \Big\{ \quad \dot{\tilde{x}}_1 = -\tilde{x}_1 \tag{38}$$

This is clearly a globally exponentially stable linear system, but since we will need a Lyapunov function to analyse this

system when $\sigma_1 \neq 0$, we use the Lyapunov function candidate $V_1(\tilde{x}_1) = \frac{1}{2}\tilde{x}_1^2$ for the analysis. The derivative of V_1 yields

$$\dot{V}_1(\tilde{x}_1) = \tilde{x}_1\dot{\tilde{x}}_1 = \tilde{x}_1(-\tilde{x}_1) = -\tilde{x}_1^2 \leq -||\tilde{x}_1||^2 \tag{39}$$

This means that the Lyapunov function satisfies

$$\begin{aligned} &k_1||\tilde{x}_1||^a \leq V_1(\tilde{x}_1) \leq k_2||\tilde{x}_1||^a \\ &\frac{\partial V_1}{\partial x} f(t,x) \leq -k_3||\tilde{x}_1||^a \end{aligned} \tag{40}$$

with $k_1 = k_2 = \frac{1}{2}$, $k_3 = 1$ and $a = 2$. Hence, by virtue of [36, Theorem 4.10], the origin for subsystem $\sum_1$ with $\sigma = 0$ is globally exponentially stable.

Analysis of subsystem 2: Subsystem $\sum_2$ has the same structure as the system in [23]; thus, we can use the results obtained in [23]. For completeness, and because we will base the further analysis on the Lyapunov function obtained here, we recall the results from [23]. In [23], the origin of the system is proven to be globally finite-time stable (GFTS) if $0 < k_m I \leq \Gamma(\cdot) \leq k_M I$, $|\varphi_1(\cdot)| \leq \alpha|\phi_1(\sigma)|$ and $|\frac{d}{dt}(\Gamma^{-1}(\cdot)\varphi_2(\cdot))| \leq \Delta$, where k_m, k_M, α and Δ are positive constants. Since the system is GFTS, it is also globally asymptotically stable [37, Proposition 3]. To prove that the origin of subsystem 2 is UGAS or globally uniformly finite-time stable, we will use [37, Theorem 12]. In the analysis, we will use the Lyapunov function found in [23], which was used to prove GFTS, but the analysis itself, i.e., proving uniformity by using [37, Theorem 12] is novel. The function $V = \xi^T P \xi$, where $\xi^T = [\phi_1(\sigma_1) \quad \sigma_2]$ and $P = \begin{bmatrix} p_1 & -1 \\ -1 & p_2 \end{bmatrix}$, $p_1 p_2 > 1$, is the generalized Lyapunov function for subsystem 2; see [23] for details. This function is globally proper and continuous (but not Lipschitz continuous on the line $\sigma_1 = 0$). For $\sigma_1 \neq 0$, this function is differentiable and

$$DV_{F(\sigma_1,\sigma_2)}(\sigma_1,\sigma_2) \leq -\mu_1\sqrt{V(\sigma_1,\sigma_2)} \tag{41}$$

where $\mu_1 > 0$ and

$$\begin{pmatrix}\dot{\sigma}_1 \\ \dot{\sigma}_2\end{pmatrix} \in F(\sigma_1,\sigma_2) = \begin{pmatrix} -k_1\Gamma(\cdot)\phi_1(\sigma_1) + \varphi_1(\sigma_1,\tilde{x}_1,t) + \Gamma(\cdot)\sigma_2 \\ -k_2\phi_2(\sigma_1) + \frac{d}{dt}\left(\Gamma^{-1}(\cdot)\varphi_2(\sigma_1,\tilde{x}_1,t)\right)\end{pmatrix} \tag{42}$$

For $\sigma_1 = 0$ and $\sigma_2 \neq 0$, we need to calculate a generalized directional derivative. Thus, consider the limit

$$D_{\{h_n\},\{u_n\}}V(0,\sigma_2) = \lim_{n\to\infty} \frac{V(h_n u_n^{\sigma_1}, \sigma_2 + h_n u_n^{\sigma_2}) - V(0,\sigma_2)}{h_n} \tag{43}$$

where $\{h_n\} \in \mathbb{K}$ ($\mathbb{K}$ is a set of all sequences of real numbers converging to zero, i.e., $\{h_n\} \in \mathbb{K} \Leftrightarrow h_n \to 0, h_n \neq 0$), $u_n = (u_n^{\sigma_1}, u_n^{\sigma_2})^T$, $\{u_n\} \in \mathbb{M}(d)$ ($\mathbb{M}(d)$ is a set of all sequences of real vectors converging to $d \in \mathbb{R}^n$, i.e. $\{u_n\} \in \mathbb{M}(d) \Leftrightarrow u_n \to d, u_n \in \mathbb{R}^n$), and $d \in F(0,\sigma_2)$. In this case, $u_n^{\sigma_1} \to \sigma_2$ and $u_n^{\sigma_2} \to q$, where $q \in [-\frac{1}{2}k_2 \pm \Delta, \frac{1}{2}k_2 \pm \Delta]$. Hence,

$$\begin{aligned} &D_{\{h_n\},\{u_n\}}V(0,\sigma_2) = \lim_{n\to\infty} \frac{V(h_n\sigma_2, \sigma_2 + h_n q) - V(0,\sigma_2)}{h_n} \\ &= \lim_{n\to\infty} \Big(p_1\big(|h_n\sigma_2|^{(1/2)}\operatorname{sgn}(h_n\sigma_2) + \beta h_n\sigma_2\big)^2 \\ &- 2\big(|h_n\sigma_2|^{(1/2)}\operatorname{sgn}(h_n\sigma_2) + \beta h_n\sigma_2\big)(\sigma_2 + h_n q) \\ &+ p_2(\sigma_2 + h_n q)^2 - p_2\sigma_2^2\Big)/h_n = -\infty \end{aligned} \tag{44}$$

Therefore,

$$D_{F(\sigma_1,\sigma_2)}V(0,\sigma_2) = \{-\infty\} \leq -\mu_1\sqrt{V(0,\sigma_2)} \text{ for } \sigma_2 \neq 0 \tag{45}$$

and the origin of subsystem 2 is therefore globally uniformly finite-time stable [37, Theorem 12], and therefore, it is also UGAS. This result implies that $||\sigma(t)|| < \beta \ \forall t \geq 0$.

Analysis of the complete system: To analyse the complete system, [35, Lemma 2.1] is used. To check whether the solutions of the complete system are uniformly globally bounded, the boundedness of $\tilde{x}_1$ must be evaluated when $\sigma_1 \neq 0$. The derivative of the Lyapunov function V_1 is then as follows:

$$\begin{aligned} \dot{V}_1(\tilde{x}_1) &= -||\tilde{x}_1||^2 + \sigma\tilde{x}_1 \leq -||\tilde{x}_1||^2 + \theta||\tilde{x}_1||^2 - \theta||\tilde{x}_1||^2 \\ &+ \beta||\tilde{x}_1|| \leq -(1-\theta)||\tilde{x}_1||^2 \quad \forall \quad ||\tilde{x}_1|| \geq \frac{\beta}{\theta} \end{aligned} \tag{46}$$

where $0 < \theta < 1$. The solutions are then UGB because the conditions of [36, Theorem 4.18] are satisfied. Consequently, the conditions of [35, Lemma 2.1] are satisfied, which implies that the origin of the complete system is UGAS. ■

One way for the inequalities in Theorem 1 to be satisfied is if the assumptions in the following theorem are satisfied.

Theorem 2: Consider the closed-loop system in (37). If the following assumptions are satisfied:

Assumption 1: The AIAUV is neutrally buoyant.

Assumption 2: The AIAUV has only revolute joints.

Assumption 3: The reference trajectory and its derivatives are continuous and bounded by design.

Assumption 4: The matrix $||\frac{d^2}{dt^2}T(\cdot)|| \leq T_M$ is bounded, where $T(\cdot)$ is defined in (15), the Coriolis-centripetal matrix is bounded by $||C(\cdot)|| \leq C_M||x_2||$ and $||\frac{d}{dt}C(\cdot)|| \leq C_m||x_2||$, the damping matrix is bounded by $||D(\cdot)|| \leq D_M||x_2||$ and $||\frac{d}{dt}D(\cdot)|| \leq D_m||x_2||$, and the matrix of gravitational and buoyancy forces is bounded by $||\frac{d}{dt}g(\cdot)|| \leq g_M||x_2||$.

Assumption 5: $\tilde{x}_2(t)$ is bounded.

then positive constants k_m, k_M, α and Δ exist such that

1) Inequality 1: $0 < k_m I \leq \Gamma(\cdot) \leq k_M I$
2) Inequality 2: $|\varphi_1(\cdot)| \leq \alpha|\phi_1(\sigma)|$
3) Inequality 3: $|\frac{d}{dt}\left(\Gamma^{-1}(\cdot)\varphi_2(\cdot)\right)| \leq \Delta$

are satisfied.

Remark 1: Assumptions 1-3 are valid due to the design of AIAUVs and their reference trajectories. Assumptions 4-5 are valid since the AIAUV is a mechanical system.

Proof: To prove that the above inequalities are satisfied, we first note some properties that arise from having revolute joints [25]:

1) Property 1: $0 < \lambda_{\min}(M) \leq ||M|| \leq \lambda_{\max}(M)$
2) Property 2: $M = M^T > 0$
3) Property 3: $\dot{M} = C + C^T$ and $\zeta^T(\dot{M} - 2C)\zeta = 0 \quad \forall \quad \zeta \in \mathbb{R}^{6+(n-1)}$

Proof of Inequality 1: $0 < k_m I \leq \Gamma(\cdot) \leq k_M I$

Since $\Gamma(\cdot) = M^{-1}(\cdot)$, we need to prove that

$$0 < k_m I \leq M^{-1}(\cdot) \leq k_M I \tag{47}$$

where k_m and k_M are positive constants. From Property 1, we have that M is lower and upper bounded; the inverse will therefore also be lower and upper bounded by $0 < 1/\lambda_{\max}(M) \leq ||M^{-1}|| \leq 1/\lambda_{\min}(M)$, which means that

$k_m = 1/\lambda_{\max}(M)$ and $k_M = 1/\lambda_{\min}(M)$. Inequality 1 is therefore satisfied.

Proof of Inequality 2: $|\varphi_1(\cdot)| \leq \alpha|\phi_1(\sigma)|$
Since $\varphi_1(\sigma, \tilde{x}_1, t) = \sigma + f_1(\cdot)\sigma + \Gamma(\cdot)(-C(\cdot)\sigma - D(\cdot)\sigma)$ with $f_1(\cdot) = \frac{d}{dt}(T(\cdot))T^{-1}(\cdot)$, we need to prove that

$$\begin{aligned} &|\sigma + f_1(\cdot)\sigma + \Gamma(\cdot)\big(-C(\cdot)\sigma - D(\cdot)\sigma\big)| \leq \\ &\alpha|\phi_1(\sigma)| = \alpha|\lceil\sigma\rfloor^{\frac{1}{2}} + \beta_{\mathrm{GSTA}}\sigma|. \end{aligned} \tag{48}$$

By rewriting

$$\begin{aligned} &|1 + f_1(\cdot) + \Gamma(\cdot)\big(-C(\cdot) - D(\cdot)\big)||\sigma| \leq \\ &\alpha|\phi_1(\sigma)| = \alpha|\lceil\sigma\rfloor^{\frac{1}{2}} + \beta_{\mathrm{GSTA}}\sigma| \end{aligned} \tag{49}$$

we find that if

$$|1 + f_1(\cdot) + \Gamma(\cdot)\big(-C(\cdot) - D(\cdot)\big)| \leq \alpha, \tag{50}$$

the inequality holds. Now, $T(\cdot)$ is a matrix that contains the rotation matrix R_B^I, the identity matrix and the expression $(1/2)(\tilde{\eta}I_3 + S(\tilde{\varepsilon}))$, which comes from $J_{k,oq}(\tilde{p})$. Since they are all bounded, the matrix $T(\cdot)$ will also be bounded. The matrix $T(\cdot)$ is also nonsingular since quaternions are used, which means that $T^{-1}(\cdot)$ exists and will also be bounded. By taking the derivative of $T(\cdot)$, we find that for $\frac{d}{dt}(T(\cdot))$ to be bounded, $\tilde{x}_2(t)$ needs to be bounded, which it is by assumption. The function $f_1(\cdot)$ is therefore a function of bounded signals, and $f_1(\cdot)$ is thus bounded. The function $\Gamma(\cdot)$ is found to be bounded in the proof of Inequality 1. The matrices $C(\cdot)$ and $D(\cdot)$ are bounded by assumption as long as $\tilde{x}_2(t)$ is bounded, which is bounded by assumption. The matrices $C(\cdot)$ and $D(\cdot)$ are therefore bounded, and since all the functions on the right-hand side of (50) are bounded, the inequality holds. Eq. (48) is therefore satisfied, and thus, Inequality 2 is satisfied.

Proof of Inequality 3: $|\frac{d}{dt}\big(\Gamma^{-1}(\cdot)\varphi_2(\cdot)\big)| \leq \Delta$
Since $\varphi_2(\sigma, \tilde{x}_1, t) = -\tilde{x}_1 + f_1(\cdot)\tilde{x}_1 + \Gamma(\cdot)(-C(\cdot)(\tilde{x}_1 + T(\cdot)\zeta_d) - D(\cdot)(\tilde{x}_1 + T(\cdot)\zeta_d) - T(\cdot)g(\cdot) - T(\cdot)M(\cdot)\dot{\zeta}_d)$, we need to prove

$$\begin{aligned} &|\frac{d}{dt}\Big(\Gamma^{-1}(\cdot)\Big(-\tilde{x}_1 + f_1(\cdot)\tilde{x}_1 + \Gamma(\cdot)\big(-C(\cdot)(\tilde{x}_1 + T(\cdot)\zeta_d) - \\ &D(\cdot)(\tilde{x}_1 + T(\cdot)\zeta_d) - T(\cdot)g(\cdot) - T(\cdot)M(\cdot)\dot{\zeta}_d\big)\Big)\Big)| \leq \Delta. \end{aligned} \tag{51}$$

By differentiating, we find that for the above to hold, we need $\frac{d}{dt}f_1(\cdot)$, $\frac{d}{dt}\Gamma(\cdot)$, $\frac{d}{dt}C(\cdot)$, $\frac{d}{dt}D(\cdot)$, $g(\cdot)$, $\frac{d}{dt}g(\cdot)$ and $\frac{d}{dt}M(\cdot)$ to be bounded since $\tilde{x}_1(t)$, $\tilde{x}_2(t)$, $f_1(\cdot)$, $\Gamma(\cdot)$, $T(\cdot)$, $M(\cdot)$, $C(\cdot)$, $D(\cdot)$, $\frac{d}{dt}(T(\cdot))$, ζ_d, $\dot{\zeta}_d$ and $\ddot{\zeta}_d$ have previously been proven to be bounded or are bounded by assumption. For the function $\frac{d}{dt}f_1(\cdot)$ to be bounded, we need for the matrix $\frac{d^2}{dt^2}T(\cdot)$ to be bounded, which it is by assumption; thus, $\frac{d}{dt}f_1(\cdot)$ is bounded. The time derivative $\frac{d}{dt}\Gamma(\cdot)$ is bounded if $\frac{d}{dt}M(\cdot)$ and $M(\cdot)$ are bounded. Since $C(\cdot)$ is bounded, $\frac{d}{dt}M(\cdot)$ is bounded (from Property 3), and $M(\cdot)$ is bounded by Property 1. The function $\frac{d}{dt}\Gamma(\cdot)$ is therefore bounded. Furthermore, $\frac{d}{dt}C(\cdot)$ and $\frac{d}{dt}D(\cdot)$ are bounded since $\tilde{x}_2(t)$ is bounded by assumption. The matrix $g(\cdot)$ is bounded since the AIAUV is neutrally buoyant, and $\frac{d}{dt}g(\cdot)$ is bounded by assumption since $\tilde{x}_2(t)$ is bounded. Now, since (51) is satisfied, Inequality 3 is satisfied. ∎

Remark 2: If the assumptions in Theorem 2 are satisfied, the inequalities in Theorem 1 are satisfied if the positive parameters α, k_m, k_M and Δ are chosen according to inequalities (47), (50) and (51) given in the proof, and the procedure in [23] can then be used to choose the gains k_1, k_2 and β_{GSTA} in (20) and (21), which will ensure the finite-time convergence.

B. System with the control law from Sec. III-B

In this section, we perform a stability analysis of the closed-loop system with the control law from Sec. III-B, i.e., the GSTA combined with the HOSMO, and show that the tracking error asymptotically converges to zero.

1) Overall closed-loop dynamics: We consider the closed-loop system (1), (13), (34). By using the facts that $\hat{x}_1 = x_1 - e_1$ and that $\hat{x}_2 = x_2 - e_2$, from Sec. III-B1, (32) is

$$\hat{\sigma} = x_1 - e_1 - x_{1,d} + x_2 - e_2 - x_{2,d} = \tilde{x}_1 - e_1 + \dot{\tilde{x}}_1 - e_2. \tag{52}$$

By rearranging, we obtain that the tracking error dynamics is

$$\dot{\tilde{x}}_1 = -\tilde{x}_1 + \hat{\sigma} + e_1 + e_2. \tag{53}$$

Furthermore, the velocity tracking error $\tilde{\zeta}$ is represented by the sliding variable $\hat{\sigma}$; cf. (27) and (32). The overall closed-loop dynamics with $\tau(\cdot)$ given by (34) is thus given by $\dot{\hat{\sigma}}$ given in (35), $\dot{\tilde{x}}_1$ given in (53) and the HOSMO error given in (29). The closed-loop dynamics is thus

$$\begin{aligned} \sum\nolimits_1 &\begin{cases} \dot{\tilde{x}}_1 = -\tilde{x}_1 + \hat{\sigma} + e_1 + e_2 \\ \dot{\hat{\sigma}} = -k_1\phi_1(\hat{\sigma}) + z \\ \dot{z} = -k_2\phi_2(\hat{\sigma}) \end{cases} \\ \sum\nolimits_2 &\begin{cases} \dot{e}_1 = -k_1|e_1|^{2/3}\,\mathrm{sgn}(e_1) + e_2 \\ \dot{e}_2 = -k_2|e_1|^{1/3}\,\mathrm{sgn}(e_1) + e_3 \\ \dot{e}_3 = -k_3\,\mathrm{sgn}(e_1) + \dot{F}(\cdot) \end{cases} \end{aligned} \tag{54}$$

2) Stability analysis:

Theorem 3: Consider the closed-loop system (1), (13), and (34). Assume that the HOSMO in (28) is used to estimate x_1 and x_2, and assume that the sliding surface is chosen as in (32). Then, the complete system is represented by the cascaded system in (54), and the origin of the cascaded system is UGAS, which ensures the asymptotic convergence of the tracking error.

Proof: Analysis of subsystem 1 with $e_1 = 0$ and $e_2 = 0$: With $e_1 = 0$ and $e_2 = 0$, subsystem 1 can be written as

$$\sum\nolimits_1 \begin{cases} \dot{\tilde{x}}_1 = -\tilde{x}_1 + \hat{\sigma} \\ \dot{\hat{\sigma}} = -k_1\phi_1(\hat{\sigma}) + z \\ \dot{z} = -k_2\phi_2(\hat{\sigma}) \end{cases} \tag{55}$$

This subsystem is then equal to the system analysed in Sec. IV-A with $\Gamma(\cdot) = 1$, $\varphi_1(\cdot) = 0$ and $\varphi_2(\cdot) = 0$, which satisfy the inequalities in Theorem 1. We can therefore conclude that subsystem 1 is UGAS.

Analysis of subsystem 2: In [31], a Lyapunov function is proposed for a third-order SMO. It is proven that the Lyapunov function is radially unbounded and positive definite and that it is a Lyapunov function for subsystem $\sum_2$, whose trajectories converge in finite time to the origin $e = 0$ for every value of $|\dot{F}(\cdot)|$ as long as $\dot{F}(\cdot)$ is bounded. Since $\dot{F}(\cdot)$ is bounded by assumptions, the origin is GFTS for every value of $\dot{F}(\cdot)$,

which means that the origin is also UGAS [37, Proposition 2 and Proposition 3], in turn implying that $||e(t)|| \leq \delta \ \forall t \geq 0$.

Analysis of the complete system: To analyse the complete system, [35, Lemma 2.1] is used. To check whether the solutions of the complete system are UGB, the boundedness of $\tilde{x}_1$ must be evaluated when $e_1 \neq 0$ and $e_2 \neq 0$, and for this purpose, the Lyapunov function candidate $V(\tilde{x}_1) = \frac{1}{2}\tilde{x}_1^2$ is used. Note that the boundedness of $\hat{\sigma}$ was proven in the proof of Theorem 1. The derivative of the Lyapunov function candidate V is then as follows:

$$\begin{aligned}\dot{V}(\tilde{x}_1) &= -||\tilde{x}_1||^2 + (\hat{\sigma} + e_1 + e_2)\tilde{x}_1 \\ &\leq -||\tilde{x}_1||^2 + \theta||\tilde{x}_1||^2 - \theta||\tilde{x}_1||^2 + (\beta + 2\delta)||\tilde{x}_1|| \\ &\leq -(1-\theta)||\tilde{x}_1||^2 \quad \forall \quad ||\tilde{x}_1|| \geq \frac{\beta + 2\delta}{\theta}\end{aligned} \tag{56}$$

where $0 < \theta < 1$. The solutions are then UGB because the conditions of [36, Theorem 4.18] are satisfied. Consequently, the conditions of [35, Lemma 2.1] are satisfied, which implies that the complete system is UGAS. ■

V. Simulation Results

In this section, we present simulation results for trajectory tracking using the control law from Sec. III-A and the control law with the HOSMO from Sec. III-B.

A. Implementation

The complete model and controllers are implemented in MATLAB Simulink. The model is implemented by using the method described in [38]. The implemented AIAUV is based on the Eelume robot, which is the robot used in the experiments reported in Sec. VI. The AIAUV has $n = 9$ links and $m = 7$ thrusters. The properties of each link are presented in Tab. I. In the thrusters column, "2: Z, Y" means that the link has 2 thrusters, one working in the z-direction and one working in the y-direction of the link. Since the robot has $n = 9$ links, it has $n - 1 = 8$ joints. All the joints were implemented as revolute joints. Joints 1, 3, 5 and 7 rotate about the z-axis, and joints 2, 4, 6 and 8 rotate about the y-axis. Since the Eelume robot has an internal joint controller,

TABLE I: Eelume link properties

Link nr.	Length [m]	Volume [m^3]	Thrusters
1	0.62	0.0158	0
2, 4, 6, 8	0.10	0.0025	0
3	0.59	0.0150	2: Z, Y
5	0.80	0.0204	3: X, X, Z
7	0.59	0.0150	2: Y, Z
9	0.37	0.0094	0

which is a P-controller, we use a P-controller for the joints in the simulations to make the simulations as similar as possible to the experiments. To create a continuous trajectory for the AIAUV to follow, we use a filter to generate a continuous trajectory between setpoints. Inverse kinematics is not used because the joint controller that is implemented on the Eelume robot is not sufficiently precise to satisfy the assumption that $q = q_d$, which is a prerequisite for the inverse kinematic control to perform properly. The thruster allocation matrix is implemented as proposed in [27].

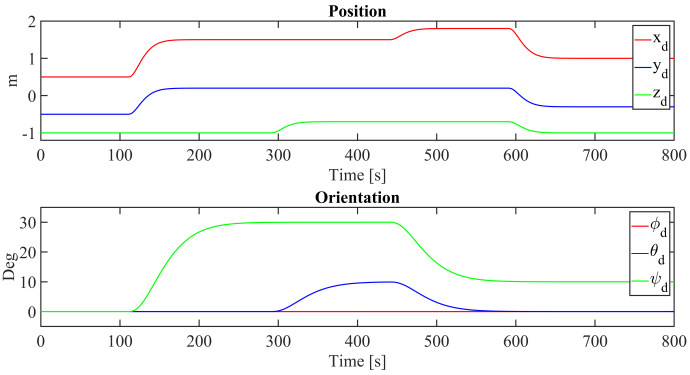

Fig. 1: Reference trajectories for position and orientation

B. Simulation cases

In this section, the different cases that were simulated are described. The cases, or shapes, chosen for the simulations are C-shape, C-shape with moving head and I-shape. The reason we chose these shapes is the two different modes, transport mode and operation mode, which is explained in detail in [27]. The transport mode is for long-distance travel, and the operation mode is for performing inspections and intervention tasks. In the transport mode, the accuracy of the tracking is not that important, and we therefore chose to use the I-shape (Sec. V-B3) for that case. In the operation mode, however, the accuracy is extremely important, and since the AIAUV is unactuated in roll when the AIAUV is in the I-shape, the I-shape cannot be used for inspection or intervention tasks. We therefore chose to test two other cases for the operation mode where all DOFs are actuated. The two cases chosen are the C-shape (Sec. V-B1) and the C-shape with moving head (Sec. V-B2). In Fig. 1 the reference trajectory for the position and orientation that is used for all the simulation cases is shown. At 100s, we change the reference for x, y and ψ, and at 300s, we change the reference for z and θ. We also change the reference for x, ψ and θ at 450s and for x, y and z at 600s. The reference values for z are, however, different for the different cases. For the C-shape, the reference for z starts at -1 and goes to -0.7, and for the C-shape with moving head and the I-shape, the z reference starts at -0.7 and goes to -0.5. The reason for the difference is that during the experiments, we observed that some of the joints were peeking out of the water and creating problems for the measurement system when we started the trajectory at -1 for the C-shape with moving head and the I-shape. The z reference for the C-shape with moving head when the control law with the HOSMO is used is also changed at 100s, starting at -1, going to -0.7 at 100s, and then to -0.5 at 300s.

1) C-shape: In the C-shape configuration, the AIAUV is shaped like a C and the AIAUV is actuated in every DOF, since the thrusters are oriented such that the robot can provide thrust in all 6DOFs. The C-shape is therefore ideal for operation mode. In C-shape the joint angles references are set to $q_d = [45\,\text{deg} \ \ 0\,\text{deg} \ \ 45\,\text{deg} \ \ 0\,\text{deg} \ \ 45\,\text{deg} \ \ 0\,\text{deg} \ \ 45\,\text{deg} \ \ 0\,\text{deg}]^T$, and in Fig. 2, the configuration of the robot is shown.

2) C-shape with moving head: The C-shape with moving head configuration of the AIAUV is similar to that of the C-shape configuration; the only difference is that the $n-1$-th and

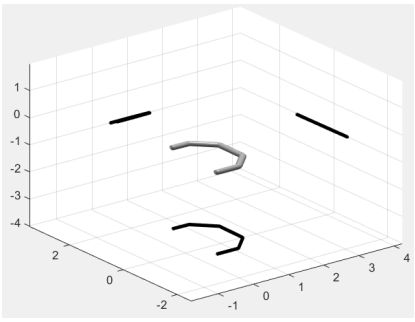

Fig. 2: Configuration in the C-shape

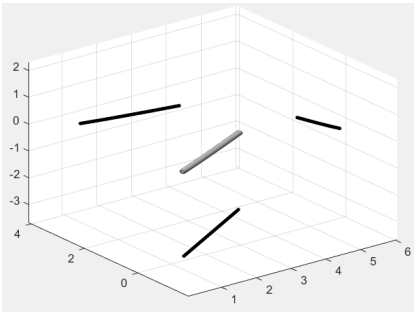

Fig. 3: Configuration in the I-shape

$n-2$-th joints are moving such that the camera positioned in the n-th joint of the AIAUV is looking around. The references for the joint angles at $t = 0$ are therefore set to $q_d(0) = [45\,\text{deg}\ \ 0\,\text{deg}\ \ 45\,\text{deg}\ \ 0\,\text{deg}\ \ 45\,\text{deg}\ \ 0\,\text{deg}\ \ 45\,\text{deg}\ \ 0\,\text{deg}]^T$, and then at 50s q_7 and q_8 starts to move in a circular motion, while the other joints remain constant. The reference for q_7 is given by four setpoints $0\,\text{deg} \rightarrow 45\,\text{deg} \rightarrow 0\,\text{deg} \rightarrow -45\,\text{deg}$. The setpoint is changed every 50s, and a filter is used to create a continuous trajectory between the setpoints. The setpoints are then repeated through the simulation. The reference for q_8 is created in the same manner, however the setpoints are then given by $45\,\text{deg} \rightarrow 0\,\text{deg} \rightarrow -45\,\text{deg} \rightarrow 0\,\text{deg}$.

3) I-shape: In the I-shape, the joints are all set to zero such that the robot is straight, like an I, i.e. the joint angles references are set to $q_d = [0\,\text{deg}\ \ 0\,\text{deg}\ \ 0\,\text{deg}\ \ 0\,\text{deg}\ \ 0\,\text{deg}\ \ 0\,\text{deg}\ \ 0\,\text{deg}\ \ 0\,\text{deg}]^T$. The configuration of the robot is shown in Fig. 3.

C. Simulations

In this section, the results from the performed simulations are presented. For the simulations, a fixed-step solver with a step size of 0.002 was used. The gains used for the simulations are those found during the experiments to ensure that the comparison between the simulations and experiments is as correct as possible. The gains for the GSTA and the HOSMO were chosen as in Tab. II. Note that we used lower gains for the I-shape than for the two other shapes, and we also used different gains for the two control schemes. The reason for that is that when the control scheme with the HOSMO was used the control input was more aggressive, which can be seen from the results. This led to higher forces being used and therefore we had to use lower gains to not experience oscillations in the experiments. Additionally, note that the gains for the HOSMO, L, are different from those used during the experiments for the C-shape and the C-shape with moving head, because we observed chattering in the simulations when we used $L = 0.01$, which was not experienced in the experiments. The results when using the control law proposed in Sec. III-A are presented in Fig. 4. Fig. 5 shows the simulation results when velocity measurements are not available and the control law proposed in Sec. III-B is used. Note that if higher gains had been used in the simulations, the results would have improved.

TABLE II: Control gains

Gains	**Tests**			
	C-shape	C-shape w/moving head	I-shape	I-shape
k_1	1	1	2	1
k_2	0.0006	0.0006	0.0006	0.0006
β	24	24	12	3
L	0.1	0.1	HOSMO not used	0.1

D. Discussion

As shown in Fig. 4 and Fig. 5, the AIAUV follows the given position and orientation very well for all three shapes, both when the control law from Sec. III-A and when the control law with the HOSMO from Sec. III-B is used. Due to the numerical solver, the sliding surface will never be exactly zero, and this might be the reason for some of the smaller deviations in Fig. 4 and Fig. 5. The AIAUV does have some issues with following the θ reference in all cases, but that might be because there is a small deviation between the desired control input and the control input that we obtain from the thruster allocation scheme, as shown in Fig. 6. Note that when we, in the simulations, gave the thruster allocation scheme more time to catch up with the reference before it was set to zero again, we observed that the reference was eventually followed. Since we want a back-to-back comparison between simulations and experiments, we kept the same timing in the simulations as in the experiments. We can also observe a small deviation in ψ at 600s for all cases, which is a transient because of the changes in position references that occur at 600s. In the I-shape, there is also a transient deviation in ψ after 100s, and the reason for this is probably the lower gains. We also observe some oscillations in θ and ψ in the C-shape with moving head case, as shown in Fig. 4c and Fig. 5c, and the reason for the oscillations is the moving head; moreover, we observe that the oscillations in the states are consistent with the movement of the head.

For the C-shape and the C-shape with moving head, we do observe an improvement in the performance when the HOSMO is used, and the reason for this improvement can be found by comparing Fig. 4b and Fig. 5b, and Fig. 4d and Fig. 5d. As shown in these plots, when the HOSMO is used, higher thruster forces are used. However, for the I-shape, comparing Fig. 4f and Fig. 5f shows that less force is used, thus making the performance in the I-shape when the HOSMO is used poorer, which is logical since lower gains are used when the HOSMO is used.

Fig. 4 and Fig. 5 also show that for both control schemes the thruster forces used are below $50N$, which is the limit of the

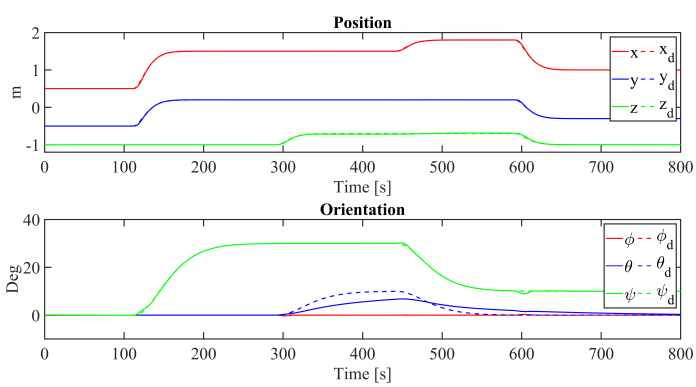

(a) Tracking in C-shape

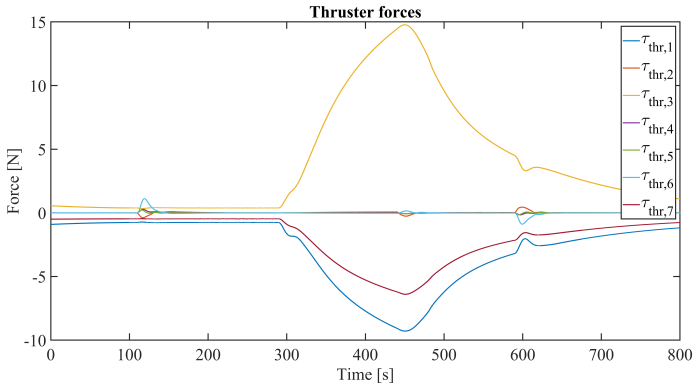

(b) Thruster forces used in C-shape

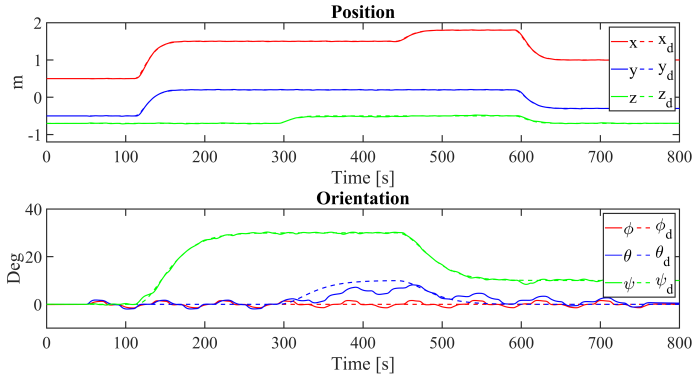

(c) Tracking in C-shape with moving head

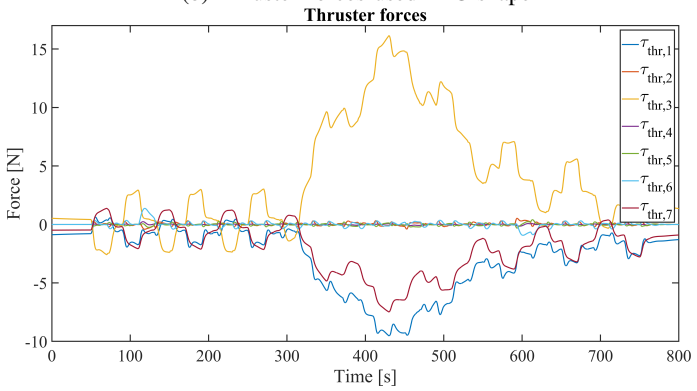

(d) Thruster forces used in C-shape with moving head

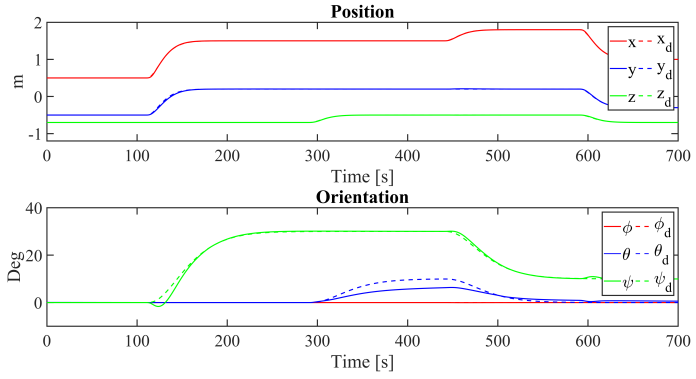

(e) Tracking in I-shape

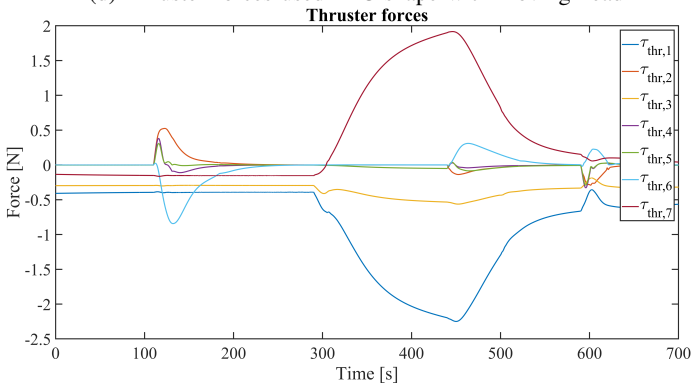

(f) Thruster forces used in I-shape

Fig. 4: Simulation results using the control law from Sec. III-A

thrusters on the actual Eelume robot. This result means that the forces used to control the AIAUV are indeed applicable.

VI. Experimental Investigation

The purpose of the experiments is to validate the theory and the robustness of the control approaches, by showing that the proposed approaches also work in experiments and not only in the ideal case presented by simulations. This section describes the Eelume robot, the experimental set-up employed for validating the proposed GSTA controllers for trajectory tracking, and the obtained results.

A. The Eelume robot

The Eelume robot used is the actual robot that the simulation model is based on, and it is described in more detail in [39]. The Eelume robot has internal joint controllers, which means that in the experiments, we could only provide a desired joint reference q_d rather than joint torque. This is also why we used a P-controller in the simulations, as explained in Sec. V-A.

B. Experimental set-up

The experiments were performed in the MC-lab at NTNU, Trondheim, Norway [40], in a tank with dimensions of length 40m, height 1.5m and width 6.45m. Real-time measurements of the position and orientation of the robot were provided by an underwater motion capture system from Qualisys [41] installed in the basin. The system consists of six identical cameras, which allow reflective markers to be tracked under water inside a working area with dimensions of 10m $\times$ 1.35m $\times$ 5.45m. Tracking the position and orientation of the AIAUV by the

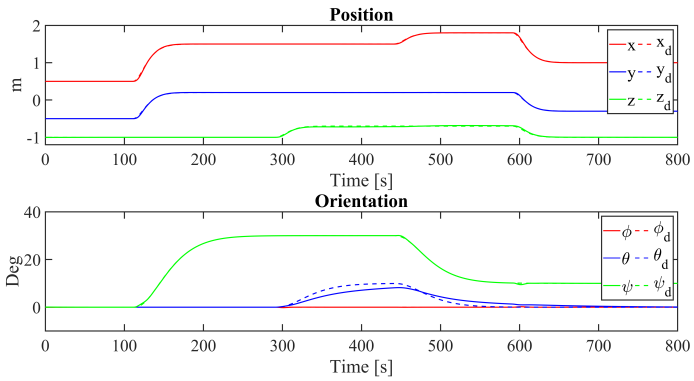

(a) Tracking in C-shape

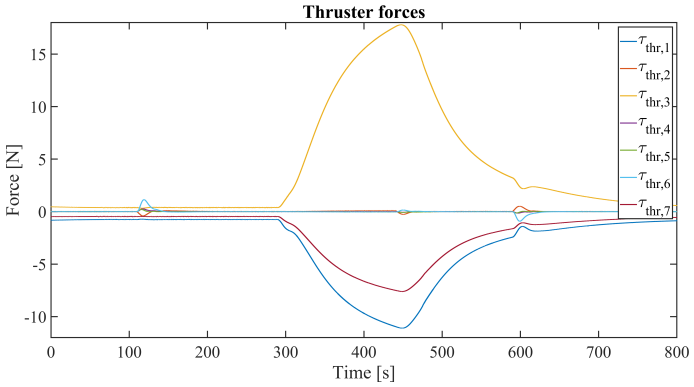

(b) Thruster forces used in C-shape

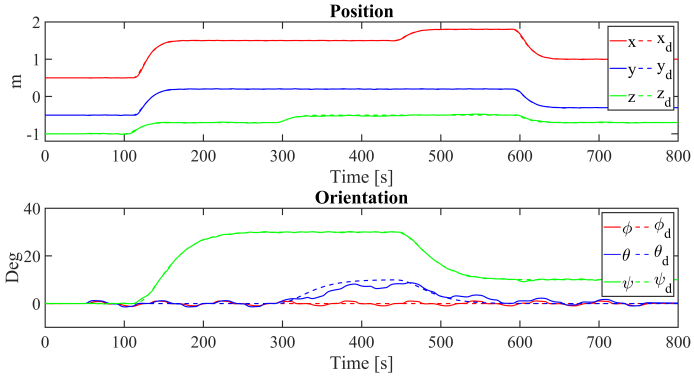

(c) Tracking in C-shape with moving head

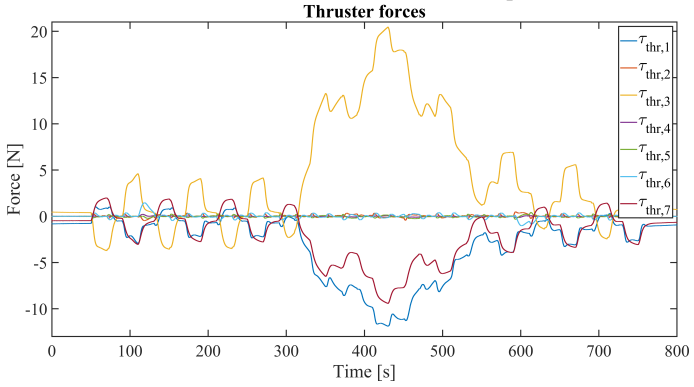

(d) Thruster forces used in C-shape with moving head

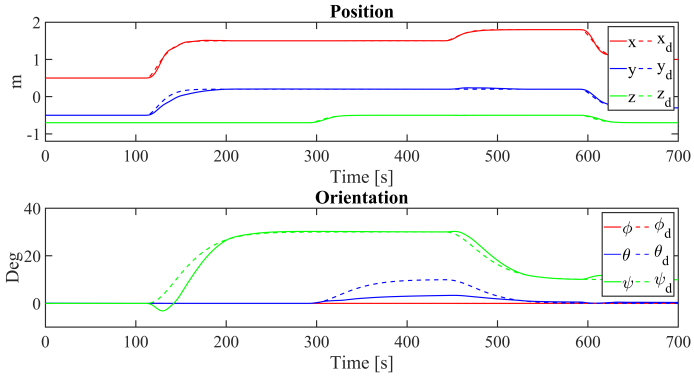

(e) Tracking in I-shape

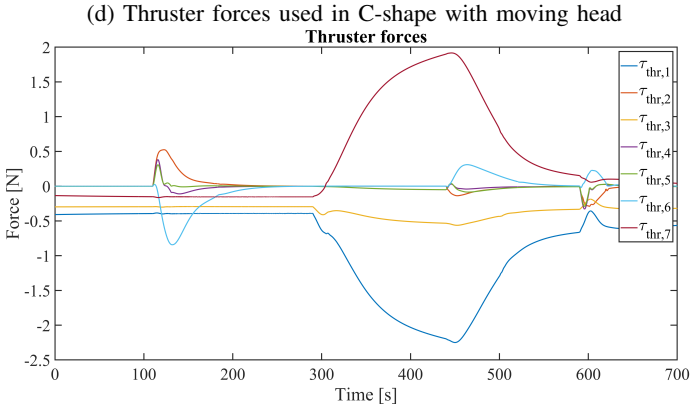

(f) Thruster forces used in I-shape

Fig. 5: Simulation results using the control law with the HOSMO from Sec. III-B

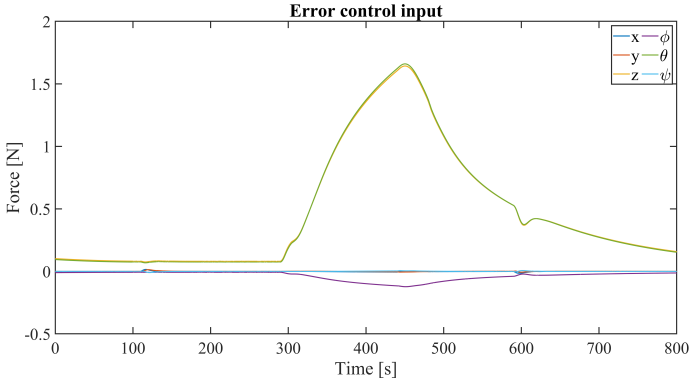

Fig. 6: Error between desired control input and actual control input from the thruster allocation scheme

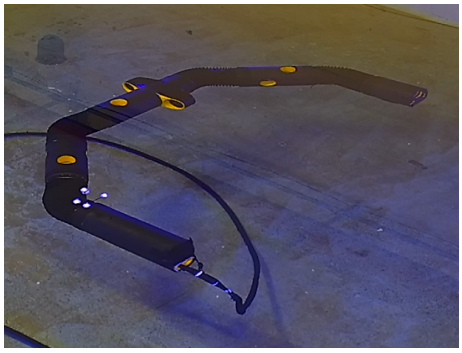

Fig. 7: The Eelume vehicle with markers attached at the base

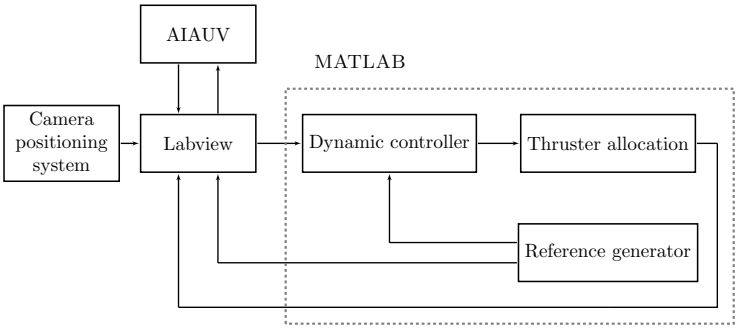

Fig. 8: Illustration of the control structure

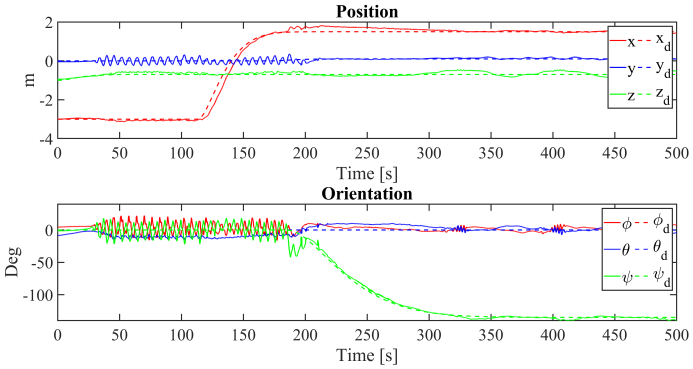

Fig. 9: Position and orientation in a complete inspection

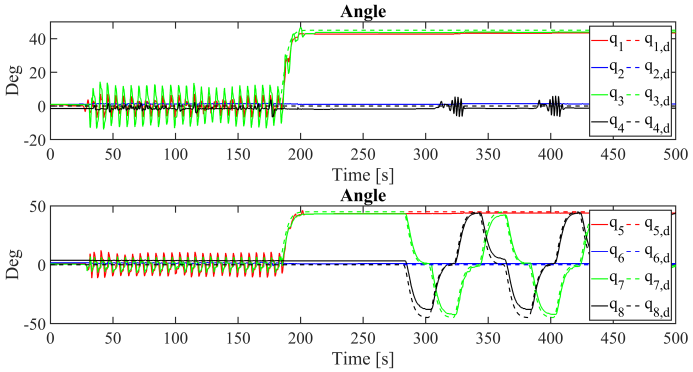

Fig. 10: Joint angles in a complete inspection

motion capture system was achieved by mounting reflective markers on the base of the robot, as shown in Fig. 7. The global frame position and orientation of the base link were measured in real time by the camera-based motion capture system. The measured position and orientation were received from an external computer to which the Qualisys system was connected, and afterwards, these measurements were sent through UDP to LabVIEW 2016. LabVIEW then sent the measurements to another computer through UDP, where the controllers and the thruster allocation algorithm were implemented in MATLAB Simulink. The thruster allocation matrix was implemented as proposed in [27]. The computer running the control structure then sent the thrust commands and the desired joint angles to LabVIEW, which passed these through an optical fibre cable to the Eelume robot. To create a continuous trajectory for the AIAUV to follow, we used a filter to generate a continuous trajectory between setpoints. Inverse kinematic control was not used, as discussed in Sec. V-A, because the internal joint controller that is implemented on the Eelume robot is not sufficiently accurate for the inverse kinematics to work properly (the assumption that $q = q_d$ is not valid). This can be observed from Fig. 10 in Sec. VI-C. The control structure used in the experiments is illustrated in Fig. 8. When the control scheme from Sec. III-A was used, an extended Kalman filter based on the kinematic model was used to estimate the linear and angular velocities. This solution was chosen since only position measurements were available in the experimental set-up. This means that we used the Kalman filter for velocity estimation in the case corresponding to the simulations where velocity measurements were available. We chose to use a Kalman filter instead of the HOSMO, because we wanted to see how the GSTA performed by itself with a standard estimator for comparison. The Kalman filter was integrated in Labview. When the control scheme with the HOSMO from Sec. III-A was used, the HOSMO was integrated in the dynamic controller.

C. Performed tests

In this section, the different tests that were performed in the experiments are explained. The tested shapes are the same as the shapes that were tested in the simulation, which were explained in Sec. V-B. The reference trajectory for the position and orientation is the same as explained in Sec. V-B. In the experiments, a test representing both modes was also performed, i.e. we started with the transport mode and then went into the operation mode. This test was mainly performed to highlight the reasoning for choosing the tests (i.e. the shapes). In the complete test, we first move forward in the x-direction in the transport mode before we turn the robot into the C-shape, and then we move in ψ to make the head face the direction that it originally was facing in the I-shape. The head is then moved around to make the test represent a complete inspection. In Fig. 9 and Fig. 10, the movement of the joints, the position and the orientation are shown. Note the oscillations when the robot is in the I-shape. These oscillations occur because the robot is underactuated in roll, which means that we do not have any thrusters that can provide a torque to control roll. The robot will therefore move from side to side in roll. Now, since the controller will try to control roll anyway, the controller calculates a force that it needs to stabilize the roll angle. This force is given to the thruster allocation algorithm to distribute to the thrusters. Since the robot is underactuated in roll, the thruster allocation scheme should have given zero as the desired moment in roll, but that is not the case. Some of the desired moment in roll is therefore distributed to the thrusters, which cause an oscillation effect. From these results, we can find that performing an inspection or intervention in the I-shape would be very difficult, or at least the precision would be bad, and we therefore move into the C-shape where the robot is still before we perform the inspection.

D. Experimental results

In this section, the experimental results from the performed tests are presented. The GSTA was easy to make work in

the experiments, and it did not require much effort in tuning. The gains were increased until we observed that rather than following the reference, the AIAUV began to oscillate around the reference. We therefore chose gains that created a small deviation from the reference rather than gains that were more aggressive (higher), where the AIAUV would oscillate around the reference. These oscillations might be caused by delays in the thrusters. The gains for the GSTA and the HOSMO were chosen as shown in Tab. II. Note that for the C-shape and the C-shape with moving head, $L = 0.01$ in the experiments. In Fig. 11 the results when using the control law proposed in Sec. III-A are presented. Note that here the velocity estimates come from the Kalman filter. In Fig. 12 we see the results when velocity measurements are not available and the control law proposed in Sec. III-B was used.

E. Discussion

In the C-shape, we observe from Fig. 11a that the reference was followed nicely, but we do observe a small deviation from the θ reference caused by a transient, i.e., when the θ reference is changed to $10\,\mathrm{deg}$ at 300s. We also observe small transient deviations in ϕ and θ at 100s, 300s and 600s, which are when the position reference is changed. These are similar to the deviations observed in the simulations. In the C-shape with moving head, Fig. 11c shows that the movement of the head caused oscillations in z, ϕ, θ and ψ, but the position reference was still followed. In the I-shape shown in Fig. 11e, we observe that the reference was followed nicely for all DOFs except ϕ, which is logical since ϕ is unactuated in the I-shape. From Fig. 11b, Fig. 11d and Fig. 11f, we find that there is some chattering in the control input, which could potentially have been reduced by reducing the gains, but if we reduced the gains, we would not obtain the desired tracking performance.

We observed an improvement in the tracking performance when the HOSMO was used without an increase in thruster use; this can be seen by comparing Fig. 11 and Fig. 12. In the C-shape, we observe from Fig. 12a that we have almost perfect tracking. In the C-shape with moving head, we observe from Fig. 12c some small oscillations in z, ϕ and θ caused by the movement of the head, but the movement is much smaller than for the case when the HOSMO is not used and is present almost only when the θ reference is changed to $10\,\mathrm{deg}$ at 300s. In the I-shape shown in Fig. 12e, we observe some deviation from the reference trajectory, but we do see that the trajectory is essentially followed. The I-shape is therefore the only case where we have worse performance with the control scheme with the HOSMO. The reason for this result is probably the lower gains, as we had oscillations in the AIAUV when we used the same gains as we did for the control law without the HOSMO, i.e., the control law from Sec.III-A. Additional measurement noise from Qualisys was observed in these tests, but the noise did not affect the performance. Thus, the conclusion would be that the HOSMO works well and creates better performance than the Kalman filter that we used. When we used the HOSMO, we observed an increase in chattering, most likely because some chattering exists in the estimated states from the HOSMO. From the HOSMO error in Fig. 13, we observe that the errors are quite small and that they appear to be noise, which means that the HOSMO is indeed applicable.

If we compare the results obtained in the simulations (Fig. 4 and Fig. 5) and the results obtained in the experiments (Fig. 11 and Fig. 12) for both control schemes, we find that they are quite similar. For the C-shape, the trajectories were almost perfectly tracked, whereas for the C-shape with moving head, we observed some oscillations in some of the states, which were caused by the moving head. For the I-shape, as expected, the tracking performance was not as good as for the other shapes since the gains used for the I-shape were lower and the AIAUV is underactuated in ϕ in this shape. For the C-shape and the C-shape with moving head, we observed an improvement in performance when the HOSMO was used, whereas for the I-shape, we found a decrease in performance. The reason for this result was probably the lower gains. For the experiments in general, we observed that the tracking performance was slightly worse than in the simulation results; however, this result is expected since in the experiments, we had outliers and errors in the position measurements. The fact that we did not have feedback from the thrusters probably also affected the errors, because we were not necessarily obtaining the forces from the thrusters that we were asking for. If we consider the difference in thruster use, we find that the main difference was more chattering in the thruster forces in the experiments. The reason for this result was probably thruster delays and measurement noise.

VII. Conclusions and Future Research

In this paper, we have proposed the generalized super-twisting algorithm for solving the trajectory tracking problem of AIAUVs in 6DOF. We have proven that the closed-loop system is uniformly globally asymptotically stable and that the generalized super-twisting algorithm gives global uniform finite-time stability, not only global finite-time stability. Comprehensive simulation and experimental results for 3 different shapes, representing both transport mode and operation mode, have been presented. The results validate and verify that the proposed approach is well suited for control of an AIAUV. Furthermore, we have also solved the trajectory tracking problem in 6DOF using the generalized super-twisting algorithm in combination with a higher-order sliding mode observer. Additionally, we have proven that the closed-loop system is uniformly globally asymptotically stable. The same 3 shapes were used to obtain comprehensive simulation and experimental results, and these validate and verify that the proposed approach is well suited for control of an AIAUV.

The simulation and experimental results were almost equally good. Some small offsets and oscillations observed in the experiments were not present in the simulations, but this is to be expected since the experiments have outliers and measurement noise. The fact that we do not have feedback on the thrusters also probably affects the results.

In the experiments, we observed an increase in performance when the higher-order sliding mode observer was used instead of the Kalman filter. Therefore, the higher-order sliding mode observer is indeed applicable for state estimation.

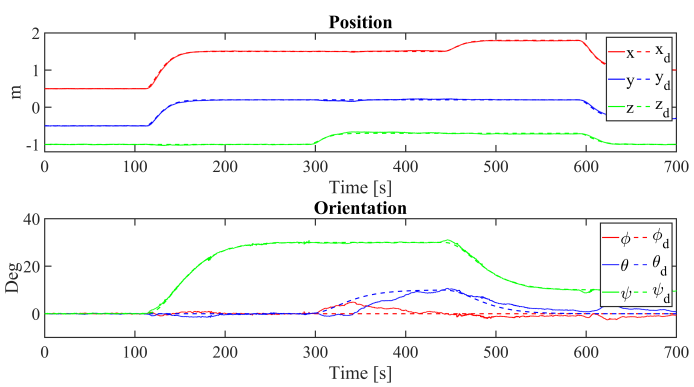

(a) Tracking in C-shape

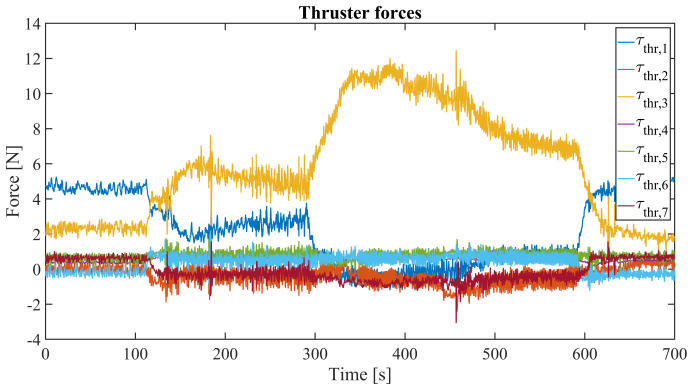

(b) Thruster forces used in C-shape

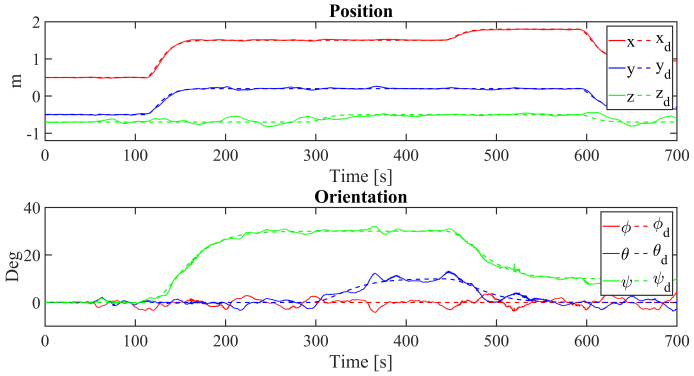

(c) Tracking in C-shape with moving head

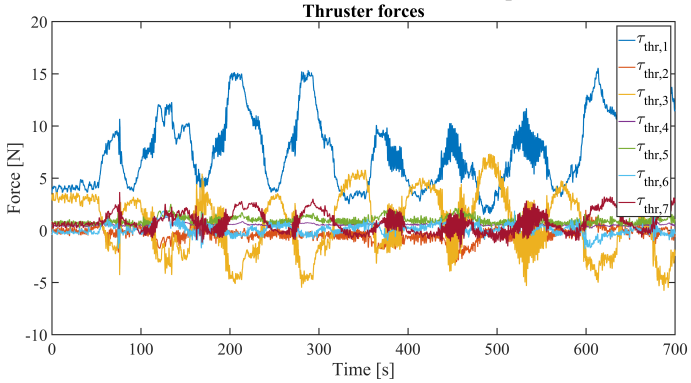

(d) Thruster forces used in C-shape with moving head

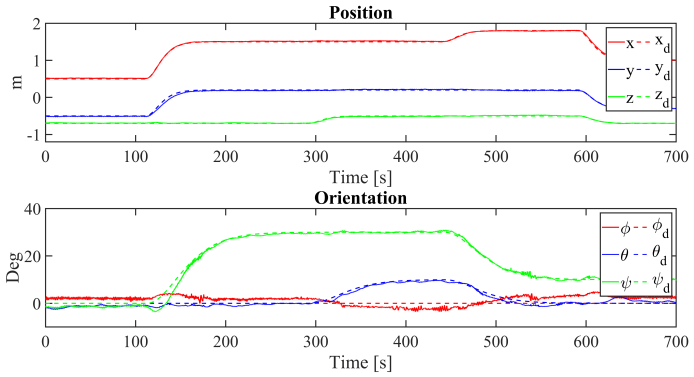

(e) Tracking in I-shape

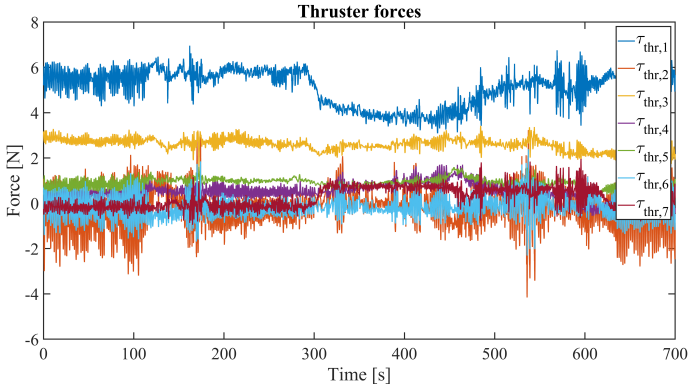

(f) Thruster forces used in I-shape

Fig. 11: Experimental results using the control law from Sec III-A

Future work includes finding and including a HOSMO that works with quaternions and comparing the proposed approaches with other existing methods.

ACKNOWLEDGMENT

This research was funded by the Research Council of Norway through the Centres of Excellence funding scheme, project No. 223254 NTNU AMOS.

REFERENCES

[1] E. Kelasidi, K. Y. Pettersen, J. T. Gravdahl, and P. Liljebäck, "Modeling of underwater snake robots," in *Proc. 2014 IEEE International Conference on Robotics and Automation.*, Hong Kong, China, May 31 - June 7 2014, pp. 4540–4547.

[2] J. Sverdrup-Thygeson, E. Kelasidi, K. Y. Pettersen, and J. T. Gravdahl, "A control framework for biologically inspired underwater swimming manipulators equipped with thrusters," in *Proc. 10th IFAC Conference on Control Applications in Marine Systems*, vol. 49, no. 23, Trondheim, Norway, Sep. 13-16 2016, pp. 89–96.

[3] ——, "The Underwater Swimming Manipulator - A Bio-Inspired AUV," in *Proc. 2016 IEEE OES Autonomous Underwater Vehicles*, Tokyo, Japan, Nov 6-8 2016, pp. 387–395.

[4] J. Liu, S. Vazquez, L. Wu, A. Marquez, H. Gao, and L. G. Franquelo, "Extended State Observer-Based Sliding-Mode Control for Three-Phase Power Converters," *IEEE Transactions on Industrial Electronics,*, vol. 64, no. 1, pp. 22–31, 2017.

[5] F. Li, L. Wu, P. Shi, and C. Lim, "State estimation and sliding mode control for semi-Markovian jump systems with mismatched uncertainties," *Automatica*, vol. 51, pp. 385–393, 2015.

[6] B. Chen, Y. Niu, Y. Zou, and B. Chen, "Adaptive sliding mode control for stochastic Markovian jumping systems with actuator degradation," *Automatica*, vol. 49, no. 6, pp. 1748–1754, 2013.

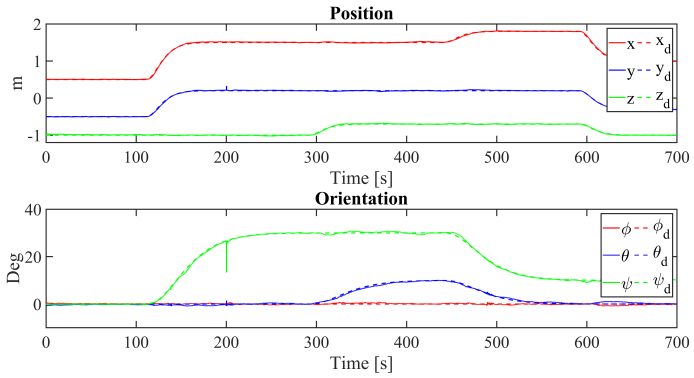

(a) Tracking in C-shape

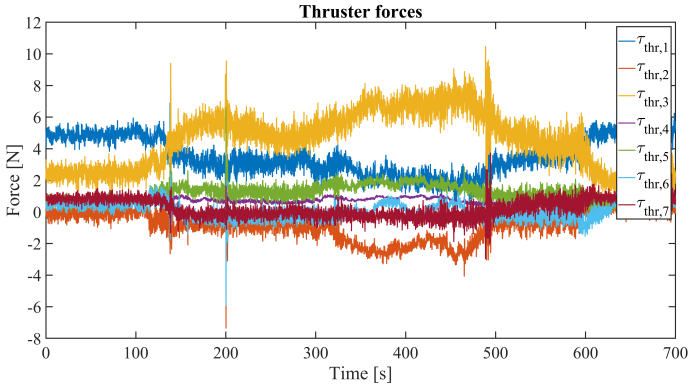

(b) Thruster forces used in C-shape

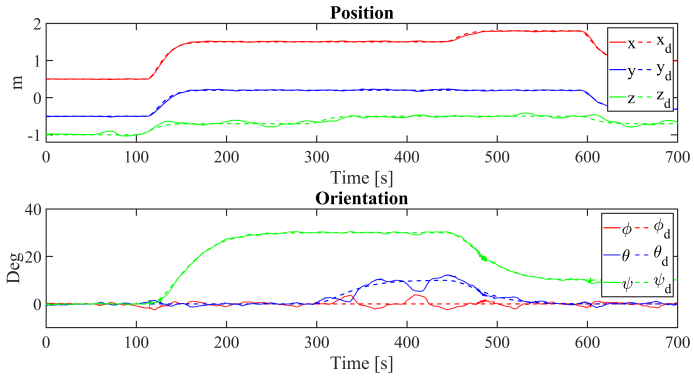

(c) Tracking in C-shape with moving head

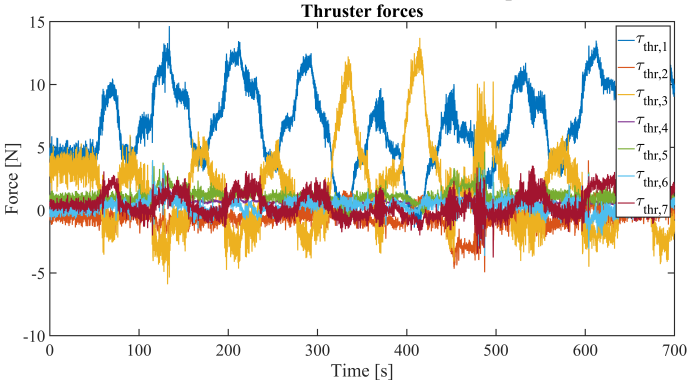

(d) Thruster forces used in C-shape with moving head

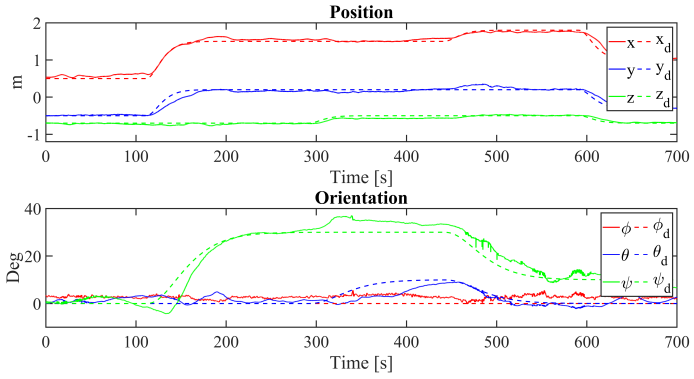

(e) Tracking in I-shape

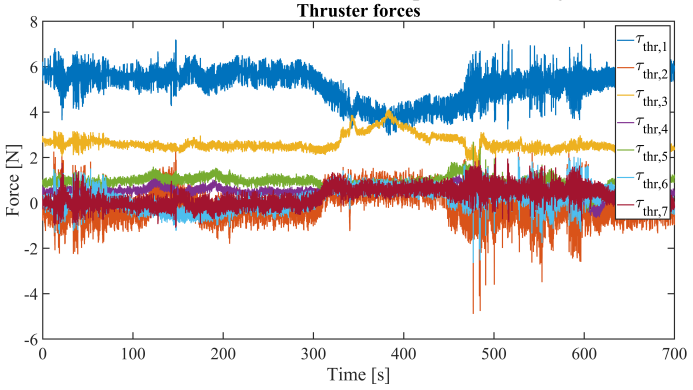

(f) Thruster forces used in I-shape

Fig. 12: Experimental results using the control law with the HOSMO from Sec. III-B

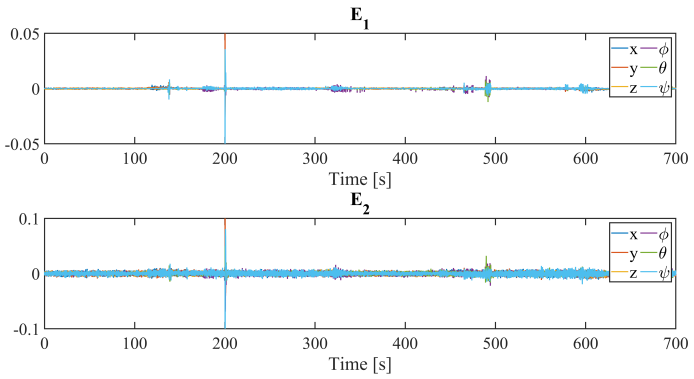

Fig. 13: Observer error when testing the C-shape

[7] W. Ligang, Z. Wei Xing, and G. Huijun, "Dissipativity-Based Sliding Mode Control of Switched Stochastic Systems," *IEEE Transactions on Automatic Control*, vol. 58, no. 3, pp. 785–791, 2013.

[8] S. Peng, X. Yuanqing, G. P. Liu, and D. Rees, "On designing of sliding-mode control for stochastic jump systems," *IEEE Transactions on Automatic Control*, vol. 51, no. 1, pp. 97–103, 2006.

[9] H. Yan, X. Zhou, H. Zhang, F. Yang, and Z. G. Wu, "A novel sliding mode estimation for microgrid control with communication time delays," *IEEE Transactions on Smart Grid*, vol. PP, no. 99, pp. 1–1, 2017.

[10] G. Antonelli and S. Chiaverini, "Singularity-free regulation of underwater vehicle-manipulator systems," in *Proc. American Control Conference*, Philadelphia, Pennsylvania, June 24-26 1998, pp. 399–403.

[11] T. I. Fossen, "Adaptive macro-micro control of nonlinear underwater robotic systems," in *Proc. 5th International Conference on Advanced Robotics*, Pisa, Italy, June 19-22 1991, pp. 1569–1572.

[12] T. I. Fossen and S. Sagatun, "Adaptive control of nonlinear underwater robotic systems," *Modeling, Identification and Control*, vol. 12, no. 2, pp. 95–105, 1991.

[13] S. Soylu, B. J. Buckham, and R. P. Podhorodeski, "A chattering-free sliding-mode controller for underwater vehicles with fault-tolerant infinity-norm thrust allocation," *Ocean Engineering*, vol. 35, no. 16, pp. 1647–1659, 2008.
[14] D. Zhu and B. Sun, "The bio-inspired model based hybrid sliding-mode tracking control for unmanned underwater vehicles," *Engineering Applications of Artificial Intelligence*, vol. 25, no. 10, pp. 2260–2269, 2013.
[15] J. Xu, M. Wang, and L. Qiao, "Dynamical sliding mode control for the trajectory tracking of underactuated unmanned underwater vehicles," *Ocean Engineering*, vol. 105, pp. 54–63, 2015.
[16] S. Liu, Y. Liu, and N. Wang, "Nonlinear disturbance observer-based backstepping finite-time sliding mode tracking control of underwater vehicles with system uncertainties and external disturbances," *Nonlinear Dynamics*, vol. 88, no. 1, pp. 465–476, 2017.
[17] M. W. Dannigan and G. T. Russell, "Evaluation and reduction of the dynamic coupling between a manipulator and an underwater vehicle," *IEEE Journal of Oceanic Engineering*, vol. 23, no. 3, pp. 260–273, 1998.
[18] E. Rezapour, K. Y. Pettersen, P. Liljebäck, and J. T. Gravdahl, "Differential geometric modelling and robust path following control of snake robots using sliding mode techniques," in *Proc. 2014 IEEE International Conference on Robotics and Automation*, Hong Kong, China, May 31 - June 7, 2014, pp. 4532–4539.
[19] Y. B. Shtessel, J. A. Moreno, F. Plestan, L. M. Fridman, and A. S. Poznyak, "Super-twisting adaptive sliding mode control: A Lyapunov design," in *Proc. 49th IEEE Conference on Decision and Control*, Atlanta, GA, USA, Dec. 15-17, 2010, pp. 5109–5113.
[20] I.-L. G. Borlaug, J. T. Gravdahl, J. Sverdrup-Thygeson, K. Y. Pettersen, and A. Loría, "Trajectory tracking for underwater swimming manipulator using a super twisting algorithm," *Asian Journal of Control*, vol. 21, no. 1, pp. 208–223, 2019.
[21] I.-L. G. Borlaug, K. Y. Pettersen, and J. T. Gravdahl, "Trajectory tracking for an articulated intervention AUV using a super-twisting algorithm in 6DOF," *IFAC PapersOnLine*, vol. 51, no. 29, pp. 311–316, Sep. 10-12, 2018, Proc. 11th IFAC Conference on Control Applications in Marine Systems, Robotics, and Vehicles, Opatija, Croatia.
[22] K. Kumari, A. Chalanga, and B. Bandyopadhyay, "Implementation of Super-Twisting Control on Higher Order Perturbed Integrator System using Higher Order Sliding Mode Observer," in *Proc. 10th IFAC Symposium on Nonlinear Control Systems*, California, USA, Aug. 23-25 2016, pp. 873–878.
[23] I. Castillo, L. Fridman, and J. A. Moreno, "Super-Twisting Algorithm in presence of time and state dependent perturbations," *International Journal of Control*, vol. 91, no. 11, pp. 2535–2548, 2018.
[24] I.-L. G. Borlaug, K. Y. Pettersen, and J. T. Gravdahl, "Tracking control of an articulated intervention AUV in 6DOF using the generalized super-twisting algorithm," in *Proc. American Control Conference*, Philadelphia, USA, Jul. 10-12 2019, pp. 5705–5712.
[25] G. Antonelli, *Underwater Robots*, 3rd ed., ser. Springer Tracts in Advanced Robotics. Springer International Publishing, 2014, vol. 96.
[26] P. J. From, J. T. Gravdahl, and K. Y. Pettersen, *Vehicle-Manipulator Systems: Modeling for Simulation, Analysis, and Control*, ser. Advances in Industrial Control. London: Springer London, 2014.
[27] J. Sverdrup-Thygeson, E. Kelasidi, K. Y. Pettersen, and J. T. Gravdahl, "The Underwater Swimming Manipulator - A Bioinspired Solution for Subsea operations," *IEEE Journal of Oceanic Engineering*, vol. 43, no. 2, pp. 1–16, 2018.
[28] T. I. Fossen, *Handbook of Marine Craft Hydrodynamics and Motion Control*. Chichester, UK: John Wiley & Sons, Ltd, 2011.
[29] J. Sverdrup-Thygeson, S. Moe, K. Y. Pettersen, and J. T. Gravdahl, "Kinematic singularity avoidance for robot manipulators using set-based manipulability tasks," in *Proc. 1st IEEE Conference on Control Technology and Applications*, Kohala Coast, Hawaii, Aug 27-30 2017, pp. 142–149.
[30] B. Siciliano and O. Khatib, *Springer Handbook of Robotics*. Berlin: Springer, 2008.
[31] J. A. Moreno, "Lyapunov function for Levant's Second Order Differentiator," in *Proc. IEEE 51st IEEE Conference on Decision and Control*, Maui, Hawaii, USA, Dec 10-13 2012, pp. 6448–6453.
[32] A. Levant, "Robust exact differentiation via sliding mode technique," *Automatica*, vol. 34, no. 3, pp. 379–384, 1998.
[33] ——, "Higher-order sliding modes, differentiation and output-feedback control," *International Journal of Control*, vol. 76, no. 9-10, pp. 924–941, 2003.
[34] A. Chalanga, S. Kamal, L. M. Fridman, B. Bandyopadhyay, and J. A. Moreno, "Implementation of super-twisting control: Super-twisting and higher order sliding-mode observer-based approaches," *IEEE Transactions on Industrial Electronics*, vol. 63, no. 6, pp. 3677–3685, 2016.
[35] A. Loría and E. Panteley, "Cascaded nonlinear time-varying systems: Analysis and design," *Lecture Notes in Control and Information Sciences*, vol. 311, pp. 23–64, 2005.
[36] H. K. Khalil, *Nonlinear Systems*, 3rd ed. Upper Saddle River, N.J: Prentice Hall, 2002.
[37] A. Polyakov and L. Fridman, "Stability notions and lyapunov functions for sliding mode control systems," *Journal of the Franklin Institute*, vol. 351, no. 4, pp. 1831–1865, 2014.
[38] H. M. Schmidt-Didlaukies, A. J. Sørensen, and K. Y. Pettersen, "Modeling of Articulated Underwater Robots for Simulation and Control," in *Proc. 2018 IEEE/OES Autonomous Underwater Vehicles*, Porto, Portugal, Nov. 6-9, 2018.
[39] P. Liljebäck and R. Mills, "Eelume: A flexible and subsea resident IMR vehicle," in *OCEANS 2017*, Aberdeen, UK, Jun. 19-22 2017.
[40] "Marine cybernetics laboratory (mc-lab)," 2018, https://www.ntnu.edu/imt/lab/cybernetics.
[41] "Qualisys-motion capture systems," 2018, https://www.qualisys.com.

Ida-Louise G. Borlaug received an MSc degree in Engineering Cybernetics at NTNU, Trondheim, Norway in 2017. She is currently a PhD candidate at the CoE Centre for Autonomous Marine Operations and Systems in the Department of Engineering Cybernetics, NTNU. Her current research interests include simulations and nonlinear control of underwater swimming manipulators with thrusters.

Kristin Y. Pettersen is a Professor in the Department of Engineering Cybernetics, NTNU, where she has been a faculty member since 1996. She was Head of the Department from 2011-2013, Vice-Head of the Department from 2009-2011, and Director of the NTNU ICT Programme of Robotics from 2010-2013. She is an Adjunct Professor at the Norwegian Defence Research Establishment (FFI). During the period 2013-2022, she is a Key Scientist at the CoE Centre for Autonomous Marine Operations and Systems (NTNU AMOS). She is a co-founder of the NTNU spin-off company Eelume AS, where she was CEO from 2015-2016.

She received MSc and PhD degrees in Engineering Cybernetics at NTNU, Trondheim, Norway, in 1992 and 1996, respectively. She has published four books and more than 250 papers in scientific conferences and journals. Her research interests focus on nonlinear control of mechanical systems with applications to robotics, with a special emphasis on marine robotics and snake robotics. She was awarded the IEEE Transactions on Control Systems Technology Outstanding Paper Award in 2006 and 2017.

She is a member of the IFAC Council and was a member of the Board of Governors of IEEE Control Systems Society 2012-2014. She has held several board positions in industrial and research companies. She is an IEEE Fellow, member of the Norwegian Academy of Technological Sciences, and member of the Academy of the Royal Norwegian Society of Sciences and Letters.

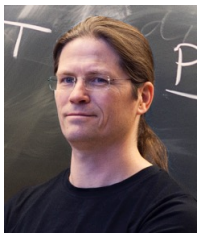

Jan Tommy Gravdahl received the Siv.ing and Dr.ing degrees in Engineering Cybernetics from the Norwegian University of Science and Technology (NTNU), Trondheim, Norway, in 1994 and 1998, respectively. He was appointed Associate Professor (2001) and Professor (2005) of the Department of Engineering Cybernetics, NTNU, where he also served as Head of the Department in 2008-09. In 2007-08, he was a Visiting Professor at The Centre for Complex Dynamic Systems and Control (CDSC), The University of Newcastle, Australia. He has supervised the graduation of 100 MSc and 12 PhD candidates. He has published five books and more than 200 papers in international conferences and journals. In 2000 and 2017, he was awarded the IEEE Transactions on Control Systems Technology Outstanding Paper Award. He is a senior editor of the IFAC journal Mechatronics. His current research interests include mathematical modeling and nonlinear control in general, in particular applied to turbomachinery, marine vehicles, spacecraft, robots, and high-precision mechatronic systems.